

1

**ETHANE IN PLANETARY AND COMETARY ATMOSPHERES:**

2

**TRANSMITTANCE AND FLUORESCENCE MODELS OF THE  $\nu_7$  BAND AT 3.3  $\mu\text{m}$**

3

4

G. L. Villanueva<sup>(1,2)</sup>

5

M. J. Mumma<sup>(1)</sup>

6

K. Magee-Sauer<sup>(3)</sup>

7

<sup>(1)</sup> Solar System Exploration Division, Mailstop 690.3, NASA Goddard Space Flight Center, Greenbelt, MD, 20771, USA. Geronimo.Villanueva@nasa.gov

<sup>(2)</sup> Department of Physics, Catholic University of America, Washington, DC 20064.

<sup>(3)</sup> Department of Physics and Astronomy, Rowan University, Glassboro, NJ 08028.

12

13

Submitted to JGR Planets on December/22/2010

14

Revised April/21/2011

15

Accepted May/9/2011

16

1    **Abstract**

2    Ethane and other hydrocarbon gases have strong ro-vibrational transitions in the 3.3  $\mu\text{m}$   
3    spectral region owing to C-H, CH<sub>2</sub>, and CH<sub>3</sub> vibrational modes, making that spectral  
4    region prime for searching possible biomarker gases in extra-terrestrial atmospheres (e.g.  
5    Mars, exoplanets) and organic molecules in comets. However, removing ethane spectral  
6    signatures from high-resolution terrestrial transmittance spectra has been imperfect,  
7    because existing quantum mechanical models have been unable to reproduce the  
8    observed spectra with sufficient accuracy. To redress this problem, we constructed a line-  
9    by-line model for the  $v_7$  band of ethane (C<sub>2</sub>H<sub>6</sub>), and applied it to compute telluric  
10   transmittances, and cometary fluorescence efficiencies. Our model considers accurate  
11   spectral parameters, vibration-rotation interactions, and a functional characterization of  
12   the torsional hot-band. We integrated the new band model into an advanced radiative  
13   transfer code for synthesizing the terrestrial atmosphere (LBLRTM), and achieved  
14   excellent agreement with transmittance data recorded against Mars using three different  
15   instruments located in the Northern and Southern hemispheres. The retrieved ethane  
16   abundances demonstrate the strong hemispheric asymmetry noted in earlier surveys of  
17   volatile hydrocarbons. We also retrieved the sensitive limits to the abundance of ethane  
18   on Mars. The most critical validation of the model was obtained by comparing  
19   simulations of C<sub>2</sub>H<sub>6</sub> fluorescent emission with spectra of three hydrocarbon-rich comets:  
20   C/2004 Q2 (Machholz), 8P/Tuttle, and C/2007 W1 (Boattini). The new model accurately  
21   describes the complex emission morphology of the  $v_7$  band at low rotational temperatures  
22   and greatly increases the confidence of the retrieved production rates (and rotational  
23   temperatures) with respect to previously available fluorescence models.

1    **1. Introduction**

2    Ground-based infrared astronomy is a powerful tool for characterizing molecular  
3    compositions of cometary and planetary atmospheres. In the 1990's, advances in infrared  
4    detectors enabled scientists to study bright infrared lines in comets and planets and to  
5    characterize their chemical compositions with unprecedented sensitivity. In 1999,  
6    commissioning of the first cross-dispersed infrared spectrometer at a large aperture  
7    telescope (NIRSPEC at Keck-2, McLean et al. 1998) closed the century that saw infrared  
8    spectroscopy transition from single element thermopiles behind low-resolution  
9    spectrographs to million-pixel detector arrays behind high-resolution spectrometers that  
10   span the entire 1-5  $\mu\text{m}$  wavelength range. Similar instruments followed quickly at other  
11   giant telescopes, together driving a revolution in molecular astronomy. The higher  
12   sensitivities and improved spectral resolution of these instruments have highlighted the  
13   limitations of current models for analyzing spectra acquired with them, and have revealed  
14   ancillary issues introduced by incomplete and/or incorrect molecular parameters. The  
15   latter problem is especially acute in the important near infrared spectral region where all  
16   aliphatic and aromatic hydrocarbons have infrared-active vibrational modes.

17   Hydrocarbon gases have strong ro-vibrational transitions in the 3.3  $\mu\text{m}$  spectral region  
18   owing to C-H, CH<sub>2</sub>, and CH<sub>3</sub> vibrational modes, making that spectral region prime for  
19   searching possible biomarker gases in extra-terrestrial atmospheres (e.g., Mars,  
20   exoplanets) and organic molecules in comets. For example, ethane has strong  $\nu_7$  and  $\nu_5$   
21   fundamental bands with origins at wavelengths (frequencies) near 3.35  $\mu\text{m}$  (2985  $\text{cm}^{-1}$ )  
22   and 3.45  $\mu\text{m}$  (2896  $\text{cm}^{-1}$ ), respectively. The discovery of abundant ethane in comet  
23   C/1996 B2 (Hyakutake) [Mumma et al. 1996], and its detection in every comet sampled

1 since then [DiSanti and Mumma 2008, Mumma & Charnley 2011, and refs. therein],  
2 created a need for accurate models of solar-pumped fluorescence for these two  
3 vibrational bands. A simple initial model for the four Q-branches seen in Hyakutake was  
4 soon extended to account for the increased number of Q-branches observed in C/1995 O1  
5 (Hale-Bopp) [Dello Russo et al 2001]. The rapid increase in power of cross-dispersed and  
6 high resolution infrared spectrometers (NIRSPEC in 1999, CRIRES in 2005) soon  
7 revealed even more spectral lines of ethane  $\nu_7$  [Mumma et al. 2001, Dello Russo et al.  
8 2006] and stimulated the first systematic study of  $\nu_5$  [Radeva et al. 2011], in comets and  
9 in Earth's atmosphere. However, the incomplete or improper accounting of ethane in  
10 public spectral databases seriously constrained the accuracy of models for telluric  
11 transmission and thus limited the achievable sensitivities for data taken using ground-  
12 based telescopes.

13 In this paper, we present a complete quantum mechanical model for the ro-vibrational  $\nu_7$   
14 band of ethane ( $C_2H_6$ ), using more accurate spectral parameters. We next discuss the  
15 limitations of molecular databases and models for synthesizing telluric atmospheric  
16 transmittance and the solar spectrum, and we present improved models for this purpose.  
17 We then obtain new line-by-line fluorescence efficiencies for ethane in space by coupling  
18 the new  $\nu_7$  band model with the solar spectrum (including Fraunhofer lines). Finally, we  
19 synthesize the terrestrial transmittance spectrum using improved molecular parameters  
20 (including ethane  $\nu_7$ ). We illustrate the increases in accuracy and sensitivity achieved, by  
21 applying these models to ground-based spectra of Mars and of comets [C/2004 Q2  
22 (Machholz), 8P/Tuttle, and C/2007 W1 (Boattini)].

23

1    **2. The Ethane model**

2    HITRAN is a comprehensive database of molecular parameters that is widely used by the  
3    spectroscopic community for synthesizing and analyzing spectra of atmospheric gases.  
4    The database undergoes regular updates and additions, and its completeness has  
5    improved greatly in recent years. The latest version [Rothman et al. 2009] contains  
6    almost 3 million lines from 42 molecules, yet the database is still not sufficient in some  
7    spectral regions. Ethane provides a good example. Even though C<sub>2</sub>H<sub>6</sub> is present in the  
8    terrestrial atmosphere at only trace amounts (0.1–2 ppbv), the lines of its strongest band  
9    ( $\nu_7$ ) are prominent in high-resolution atmospheric spectra. The latest HITRAN  
10   distribution includes parameters for some Q- branches derived by Brown et al. [1987]  
11   from ATMOS spectra, with later improvements for the <sup>P</sup>Q<sub>3</sub> sub-band from Pine and  
12   Rinsland [1999]. P- and R-branch lines are not listed. Here, we present a complete  
13   quantum mechanical band model for the  $\nu_7$  band, including lines of P-, Q-, and R-  
14   branches.

15

16    **2.1. The ro-vibrational structure**

17    For decades, laboratory scientists have extensively studied the ro-vibrational bands of  
18   C<sub>2</sub>H<sub>6</sub>, but due to the complex morphology of the ethane bands and strong spectral  
19   confusion only a limited set of spectroscopic constants have been retrieved. Ethane is  
20   composed of two methyl groups in which H-atoms of the CH<sub>3</sub> groups are sterically  
21   staggered by 60° about the C-C axis of three-fold symmetry). The molecule has twelve  
22   fundamental vibrations involving C-H and C-C stretching ( $\nu_1$ ,  $\nu_3$ ,  $\nu_5$ ,  $\nu_7$ ,  $\nu_{10}$ ),

1 deformation of the methyl group ( $\nu_2$ ,  $\nu_6$ ,  $\nu_8$ ,  $\nu_{11}$ ), torsion ( $\nu_4$ ), and bending ( $\nu_9$ ,  $\nu_{12}$ ). The  
2 perpendicular band at 3.3  $\mu\text{m}$  ( $\nu_7$ ) is infrared active and originated by stretching of the C-  
3 H bonds of individual methyl groups (see Fig. 1a). The characterization of rotational  
4 structure in this complex molecule is non-trivial because the  $\nu_7$  band is severely perturbed  
5 by overtones and combination states (with a low frequency torsional mode ( $\nu_4$ ) at  $\sim 289$   
6  $\text{cm}^{-1}$ ) that are in Fermi or Coriolis resonance with  $\nu_7$  [Pine and Lafferty, 1982]. For some  
7 K sub-bands (e.g.,  ${}^R\text{Q}_5$ ) the perturbations are so severe that the energy levels cannot be  
8 simply described using a standard power series expansion [Pine and Lafferty, 1982].

9 Description of the energy levels was performed using linear progressions of J, K and  $\ell$   
10 (where " denotes lower state and ' upper state). Considering that  $\text{C}_2\text{H}_6$  is a prolate  
11 symmetric top molecule, the quantum numbers J and K respectively indicate the total  
12 angular momentum of the molecule and its projection onto the symmetry-axis, thus  $K \leq J$   
13 (see Fig. 1b). For the ground vibrational state (see Fig. 1c) we applied the constants  
14 compiled by Pine and Lafferty 1982 (summarized in Table 1) in the form of:

$$15 \quad E''(J'', K'') = (A - B)K''^2 + BJ''(J'' + 1) - D_J J''^2 (J'' + 1)^2 - D_{JK} J''(J'' + 1)K''^2 - D_K K''^4 \quad (1)$$

16 We have had success using this simple progression for most sets of lines, but have  
17 encountered problems when trying to match the P-, R-, and Q-lines of  $K\ell''=0$  ( $\Delta K=1$ ).  
18 This difficulty indicates the limitations of this simple approximation, and a more detailed  
19 and complete model of the energies for the ground state is required to correctly model all  
20 fundamental bands of ethane. We have provisionally circumvented this problem by  
21 defining a different set of upper-state rotational constants for  $\Delta J=0$  and  $\Delta J \neq 0$  for  $K\ell'=1$   
22 [see Table 1].

1 For the upper state, Goldman et al. [1989] obtained a relatively accurate set of rotational  
 2 constants for each K-ladder using high-resolution spectra recorded by Cole et al. [1980]  
 3 and Pine and Lafferty [1982]. As described by Goldman et al. [1989], this power series  
 4 approximation of J and K does not fully characterize the complexity of the  $\nu_7$  band, but it  
 5 does achieve a reasonable precision of 0.004 to 0.010 cm<sup>-1</sup> in frequency (see Table 2 of  
 6 [Goldman et al. 1989]) for a limited number of lines. In 1996, Pine and Stone [1996]  
 7 provided refined rotational constants for a limited set of Q-lines of <sup>R</sup>Q<sub>0</sub>, <sup>P</sup>Q<sub>3</sub> and <sup>R</sup>Q<sub>3</sub>  
 8 (including splittings by torsional tunneling and A<sub>1</sub>-A<sub>2</sub> doublings). More recently,  
 9 Harrison et al. [2010] have obtained high-resolution line strengths (cross sections) for  
 10 ethane in the 3  $\mu\text{m}$  region at temperatures between 194 and 297K and total pressures  
 11 from 0.0689 Torr to 763.48 Torr. Using this dataset we identified 466 lines, which we  
 12 consolidated with 122 lines reported by Dang-Nhu et al. [1984] and 66 observed by Pine  
 13 and Stone [1996], ultimately deriving rotational constants for 30 K-ladders [see Table 1]  
 14 of the  $\nu_7$  band of ethane. The upper state energies are calculated following:

$$E'(J', K\ell') = F'_{K\ell'} + B'_{K\ell'} J'(J'+1) - D'_{K\ell'} J'^2 (J'+1)^2 + H'_{K\ell'} J'^3 (J'+1)^3 + T_{K\ell'}(J') \quad (2)$$

15 where the F, B, D and H coefficients were fitted for each K-ladder using the compilation  
 16 of lines reported above. We retrieved the third order coefficient (H) only when the  
 17 precision of line frequencies was sufficient to quantify this parameter. For some K-  
 18 ladders we observe strong perturbations, which cannot be described using a simple linear  
 19 progression. These perturbations were described using the following formula:  
 20

$$T_{K\ell'}(J') = P1_{K\ell'} \cdot (J' - P2_{K\ell'}) \cdot \exp(P3_{K\ell'} \cdot |J' - P2_{K\ell'}|) \quad (3)$$

1 where P1, P2 and P3 are the perturbation coefficients summarized in Table 1. A  
2 representation of these perturbations for  ${}^RQ_2$  is presented in Figure 2. For lines beyond  
3  $K\ell' < -8$  and  $K\ell' > 10$ , we neglect the T and H terms of equation 3, and describe the  
4 energy origins (F) and effective rotational constant (B) following Goldman et al. [1989]  
5 with:

6 
$$F' = v_0 - 2(A_S)'K'\ell' + (A' - B')K'^2 - D'_{JK}K'^4 + \eta'_{JK}K'^3\ell' \quad (4)$$

7

8 
$$B' = B_0 - D'_{JK}K'^2 + \eta'_{JK}K\ell' \quad (5)$$

9

10 in which the parameters [see values in Table 1] were fitted to all identified lines, with the  
11 exception of lines accessing  $K'' = 4, 5, 6$  which appear to be especially perturbed.

12 Using this energy model, we obtained a standard deviation of  $0.005 \text{ cm}^{-1}$  for 654 lines  
13 with quantum numbers:  $-8 \leq K\ell' \leq 10$ , and  $J' \leq 28$  (see Figure 2). These solutions do  
14 provide good results for the selected lines, but because of the numerous perturbations  
15 their validity for higher quanta and weaker spin species is uncertain. The use of  
16 individual constants for each K-ladder provides a major advance (see spectra in Figure 3),  
17 corresponding to a 36-fold improvement with respect to the  $0.18 \text{ cm}^{-1}$  standard deviation  
18 obtained using a single progression (equations 4 and 5) with the global factors in Table 1,  
19 and a 50-fold improvement to the  $0.25 \text{ cm}^{-1}$  standard deviation obtained using the global  
20 constants provided by Goldman et al. [1989]; see comparison in Figure 2.

21

1    ***2.2 Spin symmetries and spin temperature***

2    The characterization of the unique symmetries in the ethane molecule is particularly  
3    confusing, especially because different authors consider different notations depending on  
4    the assumed point group model. If internal rotation tunneling is neglected, the symmetries  
5    of the levels can be described with a point group  $D_{3d}$  (staggered) model having three spin  
6    modifications ( $A_1$ ,  $A_2$ ,  $E$ ) with ‘g’ and ‘u’ notations. In cases where torsional tunneling  
7    leads to noticeable splittings, the symmetries are best described with the  $G^+_{36}$   
8    permutation-inversion group having seven different symmetries ( $A_{1s}$ ,  $A_{4s}$ ,  $E_{1s}$ ,  $E_{2s}$ ,  $E_{3s}$ ,  
9     $E_{4s}$ ,  $G_s$ ). Symmetries of rotational levels in the ground and  $v_7$  vibrational states are  
10   presented in Table 1 for both point groups, including statistical weights ( $w''$  and  $w'$ ).  
11   Because both notations use similar letters (A, E), the reader should be careful not to  
12   confuse these definitions when examining previous publications. In this paper, we make  
13   use of both notations and distinguish between these definitions by preserving the spin  
14   label subscripts (‘g’ and ‘u’ for the  $D_{3d}$  model, and ‘s’ for the  $G^+_{36}$  model). Lines are only  
15   permitted between  $A \leftrightarrow A$ ,  $E \leftrightarrow E$  and  $G \leftrightarrow G$  levels (for both notations), and thus exchange  
16   between different spin species is normally considered negligible.

17   The spin ratios (or equivalent spin temperature, see Figure 4) can be related to the  
18   formation conditions of the molecule, and ultimately be used as a cosmogonic indicator.  
19   Unfortunately little is known about the interconversion of spin states in molecules with  
20   such high dimensional symmetry. A similar molecule ( $C_2H_4$ ) was studied by Sun et al.  
21   [2005], who observed conversions among nuclear spin isomers but no exchange in the  
22   inversion symmetry. But in the case of ethane, its molecular symmetry group does not  
23   have a unique element relating to inversion in space, as nicely summarized by Hougen

1 and Oka [2005]. Thus, the relationship between spin ratio at formation and after elapsed  
 2 times of order billions of years is uncertain; further studies will be required to properly  
 3 assess this property of the ethane molecule. As shown in Figure 4, the relationship  
 4 between  $E_g/A_g$  becomes equilibrated at very low temperatures ( $>10K$ ), much lower than  
 5 for the curves of  $H_2O$ ,  $NH_3$  and  $CH_4$ .

6

7 ***2.3. Line intensities***

8 The selection rules for the  $\nu_7$  band of ethane are:  $\Delta J = J' - J'' = +1, 0, -1$ ;  $\Delta K = K' - K'' = \ell' =$   
 9  $+1, -1$ , and  $A \leftrightarrow A$ ,  $E \leftrightarrow E$ ,  $G \leftrightarrow G$ . Line intensities  $S_\nu$  [ $cm^{-1}$  (molecule  $cm^{-2}$ ) $^{-1}$ ] between  
 10 allowed upper and lower states with  $K'' < 20$  and  $J'' < 50$  were computed as following:

11 
$$S_\nu(T) = (\nu / \nu_0) S_\nu^0(T) L_{HL}(J'', K'', \Delta J, \Delta K) F_{HW}(J'', K'', \Delta J, \Delta K) SE(\nu) Pop(E'', w'', T) \quad (6)$$

12 where  $\nu$  is the line frequency ( $E' - E''$  [ $cm^{-1}$ ]),  $\nu_0$  is the band center [ $cm^{-1}$ ],  $S_\nu^0$  is the band  
 13 intensity [ $cm^{-1}$  (molecule  $cm^{-2}$ ) $^{-1}$ , see Table 1],  $L_{HL}$  is the Hönl-London factor,  $F_{HW}$  is the  
 14 Herman-Wallis factor,  $SE$  is the stimulated emission factor and  $Pop$  is the fractional  
 15 population of the lower state.

16 The Hönl-London factor ( $L_{HL}$ ) for a perpendicular band ([Herzberg 1945, p426],  $\Delta J = J' -$   
 17  $J''$ ,  $m_L$  is 4 for  $K'' \neq 0$  or 2 for  $K'' = 0$ ) is calculated as:

$$\begin{aligned} \Delta J = 1 \quad L_{HL}(J'', K'', \Delta K) &= \frac{(J''+2+K''\Delta K)(J''+1+K''\Delta K)}{m_L(J''+1)(2J''+1)} \\ \Delta J = 0 \quad L_{HL}(J'', K'', \Delta K) &= \frac{(J''+1+K''\Delta K)(J''-K''\Delta K)}{m_L J''(J''+1)} \\ \Delta J = -1 \quad L_{HL}(J'', K'', \Delta K) &= \frac{(J''-1-K''\Delta K)(J''-K''\Delta K)}{m_L J''(2J''+1)} \end{aligned} \quad (7)$$

1 The Herman-Wallis factor ( $F_{HW}$ ) corrects for vibration-rotation interactions, since the  
2 effective dipolar operator of a molecule (and thus the intensity of a spectral line) depends  
3 not only on the total angular momentum but on vibrational operators as well. The  
4 Herman-Wallis factor was calculated as:

5

$$F_{HW}(J'', K'', \Delta J, \Delta K) = \left[ 1 + \alpha K'' \Delta K + \beta \Delta J \left( J'' + \frac{1}{2} + \frac{\Delta J}{2} \right) + \dots \right]^2 \quad (8)$$

6 where  $\alpha$  and  $\beta$  are the coefficients presented in Table 1. Stimulated emission is described  
7 with  $SE(v) = [1 - \exp(-vhc/kT)]$ , and the relative population as  $Pop(w'', E'', T) = w''$   
8  $\exp(-E''hc/kT) / Q_R(T)$ , where  $hc/K$  is the second radiation constant and  $Q_R(T)$  the  
9 rotational partition function at temperature  $T$  ( $Q_R(296K) = 51617$ ).

10 The three spectroscopic parameters that describe the intensity of the  $v_7$  band ( $S_v^0$ ,  $\alpha$  and  
11  $\beta$ ) were quantified by Dang-Nhu et al. [1984, 1987] to be  $S_v^0(296K) = 349 \pm 4.6$   
12  $\text{cm}^{-2} \text{ atm}^{-1}$ ,  $\alpha = 0.0144 \pm 0.0012$  and  $\beta = 0$  (assumed). We observe a change in the sign in  
13 the second term of the Herman-Wallis equation in Dang-Nhu et al. [1987] with respect to  
14 Dang-Nhu et al. [1984], implying a negative value of  $\alpha = -0.0144$ , that could be related to  
15 a misprint in [Dang-Nhu et al. 1987]. Using the latest cross-sections reported by Harrison  
16 et al. [2010] we retrieved  $\alpha = 0.0096 \pm 0.0020$  and  $\beta = -0.0034 \pm 0.0020$ . Our value of  $\alpha$   
17 is within  $2\sigma$  of that reported by Dang-Nhu et al. [1984].

18 The accuracy and precision of measurements of the total band intensity ( $S_v^0$ ) are directly  
19 related to the considered calibration standards, and the scheme considered to mitigate for  
20 spectral confusion. The latter is particularly crucial for ethane near  $3.3 \mu\text{m}$  since multiple  
21 fundamental (e.g.  $v_7$  and  $v_5$ ), combination (e.g.  $v_8+v_{11}$ ), and hot-bands (e.g.  $v_7+v_4 - v_4$ )

1 overlap at these wavelengths (see Figures 3 and 6). Harrison et al. [2010] have gone to  
2 great extents to obtain accurate absorption cross sections for ethane at these wavelengths,  
3 with an overall uncertainty of 4%. Their cross-sections were calibrated against PNNL  
4 spectra (Pacific Northwest National Laboratory IR database, <http://nwir.pnl.gov>), which  
5 are now considered the gold standard for ethane. Considering these new absorption cross-  
6 sections and taking into account the first torsional hot-band (see details in section 2.6),  
7 we derived a  $S_v^0$  of  $301 \text{ cm}^{-2} \text{ atm}^{-1}$  for the  $\nu_7$  band, a correction of 14% with respect to the  
8 value previously reported by Dang-Nhu et al. 1984.

9

10 **2.4 Einstein  $A_{21}$  coefficients**

11 Einstein-A coefficients were computed following Šimečková et al. [2006]:

12

$$A_{21} = \frac{8\pi cv^2 Q_{tot}(T) S_v(T)}{\left[1 - \exp(-hcv/kT)\right] \left[\exp(-E''hc/kT)\right] I_a w'} \quad (8)$$

13 where  $Q_{tot}(T)$  is the total internal partition sum (TIPS, Fischer et al. 2003) (TIPS = 70881  
14 at 296 with  $Q_v(296) = 1.3732$ ), and  $I_a$  is the isotopic abundance ( $I_a = 0.97699$  for normal  
15  $\text{C}_2\text{H}_6$ ).

16

17 **2.5 Lineshape parameters**

18 Malathy Devi et al. [2010a,b] reported an extensive and comprehensive study of line  
19 shape parameters (self- and  $\text{N}_2$ -broadening half widths and their temperature dependence)  
20 for the  $\nu_9$  band ( $825 \text{ cm}^{-1}$ ) of ethane using a multispectrum analysis of data acquired at

1 PNNL and at the Jet Propulsion Laboratory (JPL). We applied the temperature  
2 dependence of the broadening coefficients using constants reported in Table 2 of Malathy  
3 Devi et al. [2010a] for  $K'' \leq 9$  and half-width coefficients (self and  $N_2$ ) from Table 5 of  
4 Malathy Devi et al. [2010b] for  $K'' \leq 3$ . For lines accessing  $K''$  higher than the available  
5 measurements, we considered the mean progressions as presented in Figure 5. For  
6 pressure-shifts we consider the  $N_2$ -broadened pressure-induced shifts of  $-0.004 \text{ cm}^{-1}/\text{atm}$   
7 derived by Pine and Stone [1996] from  ${}^RQ_0$  and  ${}^PQ_3$ . A summary of the coefficients is  
8 presented in Table 1.

9

10 **2.6. Torsional hot-bands**

11 Ethane has a low energy torsional mode ( $\nu_4$ ) with its first excited level at  $289 \text{ cm}^{-1}$ , and  
12 thus hot-bands associated with this level ( $\nu_X + \nu_4 - \nu_4$ ) are relatively prominent at  
13 moderate temperatures. Spectroscopists have resorted to low temperatures and/or  
14 extremely high-resolution laboratory experiments to minimize/remove the confusion of  
15 hot and cold bands [e.g. Dang-Nhu et al. 1984, Pine & Stone 1996]. Using sub-Doppler  
16 molecular-beam optothermal spectroscopy, Pine and Stone [1996] resolved the complex  
17 structure of the  ${}^PQ_3$ ,  ${}^RQ_0$  and  ${}^RQ_3$  sub-bands. Their measurements revealed new  
18 absorption lines, which Pine and Rinsland [1999] attributed to a torsional hot band  
19 ( $\nu_7 + \nu_4 - \nu_4$ ,  $E_g - A_{1u}$ ) with an intrinsic intensity ( $S_{vHOT}^0$ ) of  $\sim 80\%$  to that of the  
20 fundamental ( $S_v^0$ ). Considering equation 6, the band intensity measured by Pine and  
21 Rinsland [1999] contributed  $\sim 20\%$  ( $80\% / 4$ ) of the  $\nu_7$  band at 296K, if the summed  
22 population in the first torsional level was one-fourth as large as that of the ground state at

1 296K. The hot band contribution is greatly reduced at cometary temperatures, and for  
2 instance at 100K is only 1% if we assume that vibrational populations are thermally  
3 equilibrated.

4 Unfortunately there are no spectral constants for the  $\nu_7 + \nu_4 - \nu_4$  band, and Pine and  
5 Rinsland [1999, Table 1] only provided coarse estimates for parameters of the hot  
6 analogue of the  ${}^PQ_3$  sub-band by simulating the band contour observed by Pine and Stone  
7 [1996]. The  $\nu_7 + \nu_4$ -ground ( $E_g - A_{1g}$ ) combination band is observable through Raman  
8 spectroscopy, and was tentatively detected by Fernandez et al. [2003], although the low  
9 signal to noise ratio limited the extraction of reliable rotational constants for the  $\nu_7 + \nu_4$   
10 vibrational level. Their measurements however predict the location of the hot-band to be  
11 in the 2984-2950  $\text{cm}^{-1}$  frequency range, consistent with the findings of Pine & Rinsland  
12 [1999] and with our results (Figure 6).

13 We see strong extra absorption near the Q-branches of the  $\nu_7$  band (Figure 6a, b, c). We  
14 investigated the temperature dependence of these features by integrating around ( $\pm 0.3$   
15  $\text{cm}^{-1}$ ) the strongest Q-branches, and observed that the ratio of data and model (Fig. 6d)  
16 coincided with the vibrational partition function of the  $\nu_7$  level and its first torsional  
17 component, confirming the origin of this absorption to be the  $\nu_7 + \nu_4 - \nu_4$  hot-band. We  
18 excluded the  ${}^PQ_1$  Q-branch from the analysis because it appeared slightly saturated in the  
19 Harrison et al. [2010] dataset. Due to the strong spectral confusion and complexity of this  
20 hot-band system, it is not yet possible to extract reliable constants for this hot-band  
21 system.

1 At 296K, the observed intensity of the hot-band was 25% with respect to the fundamental  
2 [ $\sum S_{v_7\text{HOT}(296K)} / \sum S_{v_7(296K)}$ ], similar to the findings of Pine and Rinsland [1999] for  
3 the  ${}^PQ_3$  replica of ~20% (see above). Perhaps, a technique as considered by Oomens and  
4 Reuss [1996] to study the  $v_7+v_9-v_9$  hot-band of ethane should be employed to fully  
5 characterize the  $v_7+v_4-v_4$  hot-band. We currently account for the existence of the hot-  
6 band in our moderate resolution spectra, by computing a simplistic  $v_7+v_4-v_4$  line-list that  
7 considers the rotational constants of  $v_4$  from Blass et al. 1990 (neglecting torsional  
8 subspecies), and fitted constants for the  $v_7+v_4$  using the data presented in Figure 6.

9

10 **2.7. Machine readable spectral atlas**

11 Following the above guidelines, we computed 17,266 spectral lines with  $K_{\max} = 20$  and  
12  $J_{\max} = 40$  in the  $2900 \text{ cm}^{-1}$  to  $3100 \text{ cm}^{-1}$  frequency range; 8,680 for the  $v_7$  band and 8,586  
13 for the hot-band. The database has been organized following the HITRAN 2008 format  
14 with line identifications following the  $G^{+}_{36}$  point group model. To allow for future  
15 investigations of conversion efficiencies between different symmetries, we report lines  
16 for each symmetry individually, even if the lines are not resolved (e.g., a  $A_{34s}-A_{12s}$  line is  
17 reported as two lines:  $A_{3s}-A_{1s}$  and  $A_{4s}-A_{2s}$ ). The vibrational indicators are V7, GROUND,  
18 V7+V4 and V4; while the local quantum numbers are  $J$   $K$  and  $\ell$ . The atlas for the  $v_7$   
19 band has been provided to the HITRAN team for further integration into their  
20 consolidated database. Due to the large uncertainty in the rotational constants of the hot-  
21 band, we will only provide the atlas of the hot-band upon request, and to be used with  
22 moderate resolution spectra only.

1    **3. Modeling of ethane in terrestrial atmospheres (LTE case)**

2    Ground-based spectra of extraterrestrial and cometary atmospheres are affected by  
3    telluric absorption. The incoming spectral lines are often Doppler-broadened and they  
4    experience extinction by atmospheric lines that may themselves approach the Doppler-  
5    broadened limit (e.g., gases with significant stratospheric and mesospheric components,  
6    such as CH<sub>4</sub>, CO<sub>2</sub>, and O<sub>3</sub>). Analysis of spectra measured for such lines requires that  
7    telluric transmittance be synthesized at sub-Doppler resolution (a spectral resolution of  
8    not more than 100 m/s, or 0.001 cm<sup>-1</sup> at 3000 cm<sup>-1</sup>). We applied the new model for C<sub>2</sub>H<sub>6</sub>  
9    ( $\nu_7$  and torsional hot-band) to synthesize terrestrial spectra using an advanced radiative  
10   transfer code for the terrestrial atmosphere that accesses a customized database of  
11   spectral constants from 42 molecules including C<sub>2</sub>H<sub>6</sub> [see Fig. 7 and Appendix A].

12   Proper synthesis of terrestrial spectra requires line-by-line, layer-by-layer radiative  
13   transfer modeling of the atmosphere, in which the quality of the synthesized spectrum  
14   depends directly on the robustness of the used set of radiative transfer equations, the  
15   precision of the adopted spectroscopic constants, and the accuracy of the assumed  
16   atmospheric conditions (Fig. 8 - P(z), T(z), abundance profiles, and geometrical  
17   conditions). Until 2005 we used the Spectrum Synthesis Program (SSP, [Kunde and  
18   Maguire 1974]) accessing the HITRAN 1992 [Rothman et al. 1992] to compute terrestrial  
19   spectra. From 2005 until 2009, we used the more advanced GENLN2 v4 model [Edwards  
20   1992], which provides highly realistic and Doppler-limited spectral synthesis of the  
21   terrestrial atmosphere. We improved the GENLN2 v4 model by providing a correction to  
22   properly account for spectral pressure-shifts, and introducing the capability to access the

1 latest HITRAN databases [Villanueva et al. 2008a]. However, GENLN 2 is no longer  
2 supported by NCAR (National Center for Atmospheric Research).

3 In 2005, a new efficient line-by-line radiative transfer became available, the LBLRTM  
4 (Line-By-Line Radiative Transfer Model) [Clough et al. 2005]). Perhaps, one the biggest  
5 advantages of this code relative to GENLN2, is that it is highly optimized, allowing us to  
6 increase the number of layers and the number of spectral points for the same computation  
7 time, ultimately achieving a more realistic atmospheric solution. In addition, this code is  
8 maintained by AER (Atmospheric and Environmental Research, Inc.) and has been (and  
9 continues to be) extensively validated against atmospheric spectra from the ultraviolet to  
10 the sub-millimeter. Even though the AER team provides a compiled spectral database to  
11 use with its LBLRTM, we have preferred to instead use the more universally recognized  
12 HITRAN atlas as the base for our radiative transfer modeling (using LBLRTM) with our  
13 own corrections and updates tailored to our requirements [see Appendix A].

14 Using our updated spectral database and LBLRTM, we synthesized spectra for the  
15 complete L-band [2.8 – 4.2 $\mu$ m, Fig. 7], with a spectral resolution of 0.0005 cm<sup>-1</sup> and  
16 consistent with a mean sampling power of ~5 million ( $\lambda/\Delta\lambda$ ), or a velocity resolution of  
17 60 m s<sup>-1</sup>. This novel method has been successfully applied to calibrate and process  
18 infrared spectra of planets [Figs. 9 and 10] and comets [Figs. 12, 13 and 14] taken with  
19 several instrument/telescope combinations (see Section 5).

20 Even though we obtain very good results with our ethane  $v_7$  band model, the line list is  
21 based on a restricted set of spectral constants and this ultimately leads to limited precision  
22 and accuracy. These imprecisions could cause assignment of improper transmittance

1 values for some incoming ethane lines due to accidental overlap with Doppler-broadened  
2 lines of stratospheric O<sub>3</sub>. Further empirical studies will be needed to properly characterize  
3 the complete structure of this band, including a full description of torsional tunneling  
4 splittings, overtone perturbations, hot-bands, and A<sub>1</sub>-A<sub>2</sub> doublings for all K sub-bands.  
5 We intend to expand our model as more complete ethane line parameters are obtained.

6

7 **4. Modeling of ethane in cometary atmospheres (non-LTE case)**

8 The C<sub>2</sub>H<sub>6</sub> ν<sub>7</sub> band is particularly bright in hydrocarbon-rich comets where efficient solar  
9 pumping (and inefficient collisional quenching) leads to strong C<sub>2</sub>H<sub>6</sub> fluorescence  
10 emission. The complexity of the band in comets is revealed in Figures 12, 13 and 14. The  
11 torsional mode is inactive to radiative decay and little is known about its possible  
12 collisional quenching or excitation. It is possible that the vibrational partitioning (of ν<sub>4</sub>)  
13 imparted upon release at the cometary nucleus is maintained throughout the inner coma,  
14 and thus the torsional manifold could become increasingly disequilibrated from the  
15 rotational and kinetic distributions as the gas flows outward through the coma, ultimately  
16 permitting pumping from the torsional level and leading to ν<sub>7</sub> hot-band fluorescent  
17 emission. Our cometary data show no evidence of strong hot-band emission, but higher  
18 spectral resolution and a better understanding of the spectral character of the hot-band  
19 will be necessary to test its contribution or lack thereof to the total flux in the ν<sub>7</sub> region.

20 Collision partners in cometary atmospheres usually lack sufficient energy to excite  
21 vibrational transitions and the rate of quenching collisions is much smaller than radiative  
22 decay rates for (infrared active) excited states. Thus, the vibrational manifold is not

1 populated in LTE (local thermodynamic equilibrium). Instead, solar radiation pumps the  
2 molecules into an excited vibrational state, which then de-excites by rapid radiative  
3 decay. Infrared photons are emitted through decay to the ground vibrational state, either  
4 directly (resonant fluorescence) or through branching into intermediate vibrational levels  
5 (non-resonant fluorescence). Resonance fluorescence is the expected dominant factor in  
6 the excitation and the sole pumping mechanism we consider here, although additional  
7 excitation cascading from levels with energies higher than  $v_7$  may also be active. We  
8 expect to expand the excitation for non-resonant fluorescence of the model, once  
9 spectroscopic data of related bands become available.

10 Since fluorescence is a non-LTE process, computation of line-by-line fluorescence  
11 efficiencies (g-factors) entails the building of a full quantum mechanical model. This  
12 requires precise knowledge of the rotational structure (energy levels) for each vibrational  
13 level involved, statistical weights, selection rules, perturbations (e.g. Coriolis effects,  
14 splittings, tunneling) and band emission rates. The difficulty of this task has limited the  
15 development of new models, particularly for those molecules having a complex  
16 symmetry structure, and consequently only a limited set of line-by-line fluorescence  
17 emission models are currently available. In the case of C<sub>2</sub>H<sub>6</sub>, previous attempts to model  
18  $v_7$  fluorescence in comets focused only on integrated Q-branch intensities but did not  
19 specify the fine rotational structure, aside from adopting a specific rotational temperature  
20 [Mumma et al. 1996, Dello Russo et al. 2001].

21 Another problem with most current cometary (infrared) fluorescence models is that they  
22 often assume the source for solar pumping is a simple black-body continuum with an  
23 effective temperature of the Sun. This approximation is somewhat correct for the

1 continuum flux at certain wavelengths ( $2900 - 3300 \text{ cm}^{-1}$ ), but it leads to inaccuracies  
2 when computing pumping rates for individual ro-vibrational lines if the relative  
3 heliocentric velocity of the comet shifts the pumping radiation field into solar absorptions  
4 [Swings effect]. Omitting this effect will introduce not simply a relative error, but will  
5 lead to incorrect retrievals of rotational and spin temperatures, since these are derived  
6 from line-to-line intensity ratios. We replace the adopted blackbody radiation field with a  
7 synthesis of the true solar spectra using a combination of empirical parameters from the  
8 solar spectrum [Hase et al. 2006; 2010] calibrated with a stellar continuum flux model  
9 [Kurucz 1997]; see Appendix B for a full discussion.

10 Fluorescence emission rates (g-factors) are normally quantified as energy (or quanta)  
11 emitted per second per molecule in units of [ $\text{J s}^{-1} \text{ molec}^{-1}$ ], [ $\text{W molec}^{-1}$ ], [ $\text{photon s}^{-1}$   
12  $\text{molec}^{-1}$ ] or simply [ $\text{s}^{-1}$ ], and are computed following a two-step process: 1) pumping to  
13 the excited state and 2) relaxation to lower levels. The spectral constants needed to  
14 compute g-factors can be extracted from an atlas of molecular lines, like HITRAN, if the  
15 tabulated data are adequate. When validated, these databases are extremely valuable  
16 repositories of the latest spectral constants and of line parameters that can be influenced  
17 by complex perturbations such as Coriolis effects, splittings, resonances and tunneling.  
18 Consequently we developed a General Fluorescence Model (GFM) to compute  
19 fluorescence emission rates (see Appendix C), and applied it to our ethane line lists (hot  
20 and cold  $\nu_7$  bands) by creating a complete atlas for this band system (as reported in  
21 Section 2). Apart from  $\text{C}_2\text{H}_6 \nu_7$  (Table 1) and  $\nu_5$  (Radeva et al. 2011), we successfully  
22 applied this approach to other infrared band-systems ( $\nu_1$  of HCN,  $\nu_3$  of  $\text{CH}_4$ , 1-0 bands of  
23 CO and  $^{13}\text{CO}$ ,  $\nu_1$  and  $2\nu_2$  of HDO,  $\nu_3$  and  $\nu_2+\nu_4+\nu_5$  of  $\text{C}_2\text{H}_2$ , Villanueva et al. in prep.).

1

2    **5. Discussion of Models and Fluorescence Efficiency**

3    ***5.1. LTE Validation: Results from Ground-based Measurements***

4    We validate our synthetic terrestrial models by comparing them to infrared spectra of  
5    Mars and comets acquired with different spectrometer/telescope combinations: CRIRES  
6    (CRyogenic high-resolution InfraRed Echelle Spectrograph [Käufl et al. 2004]) at the  
7    VLT (Very Large Telescope) in Chile, CSHELL (Cryogenic Echelle Spectrometer  
8    [Tokunaga et al. 1990]) at the NASA-IRTF (InfraRed Telescope Facility) in Hawaii, and  
9    NIRSPEC (Near-InfraRed Echelle SPECtrograph [McLean et al. 1998]) at the Keck II  
10   Telescope in Hawaii.

11   In August 2009 we observed Mars using the CRIRES instrument, sampling the planet at  
12   its mid-afternoon along meridian longitudes passing through Syrtis Major (an ancient  
13   shield volcano) and the Hellas impact basin (geometry shown in Fig. 11a). These  
14   observations reveal the recently discovered CO<sub>2</sub> band (Mars), multiple lines of water  
15   (Mars, Earth), and the telluric absorption spectrum of the v<sub>7</sub> band of C<sub>2</sub>H<sub>6</sub> (Fig. 9). In  
16   January 2006, we sampled Mars at its mid-morning along meridian longitudes passing  
17   through Valles Marineris and the Argyre impact basin (geometry shown in Figs. 11b-c)  
18   using two CSHELL settings obtained on two consecutive days (Fig. 10).

19   For each observatory, we synthesized terrestrial transmittance and radiance spectra for  
20   C<sub>2</sub>H<sub>6</sub> and other species by assuming default geometrical conditions for that high-altitude  
21   site, assuming clear atmospheric conditions (no aerosols), 50 (optically thin) atmospheric  
22   layers, and LTE populations. The atmospheric conditions (pressure, temperature and

1 abundances) are based on a standard tropical profile (Fig. 8), modified to describe the  
2 observing conditions through two temperature parameters (T1 and T2), a pressure scaling  
3 factor (PF) and abundance factors (AF, see profiles for CH<sub>4</sub> and C<sub>2</sub>H<sub>6</sub> in Fig. 8c). The  
4 given pressure profile is scaled following  $P'(z) = P(z) \times PF$ , while the temperature profile  
5 is divided into tropospheric (affected by T1) and stratospheric (affected by T2, see Fig.  
6 8a) sectors. The abundance profiles are scaled relative to the tropical profile by a  
7 molecular multiplier relative to the tropical value. For each dataset, we retrieved  
8 abundances and the atmospheric parameters (T1, T2, PF) using a Levenberg-Marquardt  
9 non-linear-minimization algorithm that compares the transmittance model to the  
10 absorption features observed against the planetary continua.

11 Agreement of the terrestrial ethane residuals and synthesized spectra is very good, and  
12 reveals strikingly different C<sub>2</sub>H<sub>6</sub> abundances at Mauna Kea in Hawaii and Cerro Paranal  
13 in northern Chile. In particular, the CH<sub>4</sub> abundance was nominal for both sites, but the  
14 C<sub>2</sub>H<sub>6</sub> abundance showed important seasonal variations and extremely low values for the  
15 Southern hemisphere. At first, we were concerned that inaccuracies of the  $\nu_7$  band model  
16 introduced these excursions, but earlier independent investigations confirm our retrievals  
17 [e.g. Rinsland et al. 2002, Glatthor et al. 2009]. For instance, the recent study of Helmig  
18 et al. [2009] reports similar trends from a vast global monitoring program of volatile  
19 organic compounds (VOCs), including C<sub>2</sub>H<sub>6</sub>. Both CH<sub>4</sub> and C<sub>2</sub>H<sub>6</sub> mostly arise from  
20 biogenic and anthropogenic emissions, although methane has a much longer lifetime (~8  
21 years) than ethane (months, see Hough 1991) in the terrestrial atmosphere.

22 The short ethane lifetime causes important fluctuations in its atmospheric concentration,  
23 since the sources and sinks vary geographically, and seasonally. This is particularly

1 evident in the Southern hemisphere where anthropogenic emissions are much smaller,  
2 leading to a C<sub>2</sub>H<sub>6</sub> maximum 7 times lower than in the Northern hemisphere [Helmig et al.  
3 2009], consistent with our findings [see Table 2]. At the summit of Mauna Kea, we  
4 observe an equivalent volume mixing ratio (VMR) of 1 ppb, similar to that of Rinsland et  
5 al. [1994] (1.1 ppb) for Mauna Loa at this season. The retrievals from Rinsland et al.  
6 [1994] were based on the  $\nu_7$  <sup>P</sup>Q<sub>3</sub> sub-branch of ethane, but ignored the presence of the  
7 hot-band absorption from the  $\nu_7 + \nu_4 - \nu_4$  band [Pine and Rinsland 1999] at these  
8 frequencies. If we attempt to revise the values from Rinsland et al. [1994] considering  
9 hot-band absorption and the new band intensity from PNNL spectra, their VMR would  
10 become ~1 ppb, in excellent agreement with our results. These consistencies together  
11 with the excellent agreement we obtained when we compared the synthetic models to  
12 spectra taken using different instruments (Figs. 9, 10, 12, 13, 14) are important  
13 validations of the  $\nu_7$  line-by-line model (including our updated spectral database) and the  
14 radiative transfer modeling.

15 By properly accounting for the telluric absorption of C<sub>2</sub>H<sub>6</sub> in this spectral region, we  
16 obtain better quality residuals, ultimately allowing us to perform very sensitive searches  
17 for biomarker gases on Mars and other astronomical objects. Using the residuals  
18 presented in Figures 9 and 10, we obtained the most sensitive upper-limits for ethane on  
19 Mars ever measured [see Table 2]. We can expect immediate improvement in these  
20 upper limits by including additional spectral scans.

21

22 **5.2. Solar Spectrum: Extraterrestrial and Cometary Spectra**

1 The precise modeling of the solar spectrum is particularly important when observing  
2 planetary bodies in reflected light (e.g., Mars, Moon). The infrared radiation observed  
3 from Mars is a combination of reflected sunlight (with Fraunhofer lines) and planetary  
4 thermal emission (featureless continuum). Sparse spectral lines of Mars' atmospheric  
5 constituents are superposed on the continua according to the optical path experienced by  
6 the two components [see Figs. 9 and 10]. Sunlight experiences a double optical path  
7 (Sun-to-surface + surface-to-Observer), while the Mars "thermal" continuum traverses  
8 only a single path (surface-to-observer). We determine the relative contributions of solar  
9 and thermal emission to the measured continuum by comparing the measured area  
10 (equivalent width) of Fraunhofer lines with their true value (see Appendix A). This  
11 permits identification of the "effective" optical path needed to properly determine  
12 molecular abundances on Mars (see details in Villanueva et al. 2008a, Novak et al. 2003),  
13 and thus an accurate solar model has impact not only on the spectral residuals but also on  
14 the retrieval process.

15 The signal-to-noise ratio (SNR) of the adopted solar spectrum limits the maximum  
16 achievable quality of the residuals. At 3  $\mu\text{m}$  the typical SNR of the ATMOS solar  
17 spectrum [Abrams et al. 1996] is  $\sim$ 1000 ( $1\sigma$ ), a sensitivity achievable in minutes with  
18 most bright infrared sources (e.g., Mars, flux standard stars) using current high-resolution  
19 spectrometers.

20 To increase the SNR of the residuals, we combined empirical and observational data from  
21 ground-based and space-based instruments to obtain an improved model for the solar  
22 spectrum (see Appendix B). This new solar spectrum will greatly contribute to the search  
23 for weak spectral signatures within solar reflected sunlight; this is demonstrated with

1 Figs. 9 and 10, where we observe excellent agreement between the solar features  
2 imprinted in the Mars continua and those synthesized with the new solar model.

3 The precise description of solar features is of paramount importance when studying solar  
4 pumped fluorescence in comets. The use of a non-realistic solar pumping flux would  
5 introduce errors up to 30% for certain g-factors of the  $v_7$  band of  $C_2H_6$ , and up to 40% for  
6 selected lines of the 1 – 0 band of CO, for example. Because this (Swings) effect is  
7 dependent on the heliocentric velocity of the comet, fluorescence rates need be computed  
8 for each orbital situation using the synthesized solar spectrum described in equation C-3.

9

### 10 **5.3. Validation of Fluorescence Efficiency Factors - Comets**

11 We have chosen three cometary datasets (8P/Tuttle, C/2007 W1 (Boattini), C/2004 Q2  
12 (Machholz)) to test the new  $C_2H_6$  fluorescence model. These comets displayed bright  
13 ethane emissions and different rotational temperatures, in spectra acquired with CRIRES  
14 and NIRSPEC. Comet 8P/Tuttle (8P hereafter) was observed in Jan-Feb 2008 using  
15 CRIRES at the VLT with the adaptive optics (AO) system [Fig. 12]. Using AO  
16 minimizes slit-losses and achieves an increased signal-to-noise in the central part of the  
17 coma. The spatial resolution along the slit is high as well and is close to the diffraction  
18 limit of the telescope.

19 Results for six volatiles including  $C_2H_6$  were presented in Böhnhardt et al. [2008]. At the  
20 time of observations (26 January 2008), the cometary ephemerides were:  $r_h = 1.03$  AU  
21 (heliocentric distance),  $v_h = -0.37$  km s<sup>-1</sup> (heliocentric velocity of the comet),  $\Delta = 0.49$   
22 AU (geocentric distance),  $v = 24.7$  km s<sup>-1</sup> (geocentric velocity of the comet); and (as

1 retrieved from 19 water lines) the nucleus-centered rotational temperature was  $60^{+8}_{-9}$  K  
2 for H<sub>2</sub>O. We synthesized a fluorescence model for C<sub>2</sub>H<sub>6</sub> for the above mentioned  
3 conditions, and retrieved a C<sub>2</sub>H<sub>6</sub> production rate of  $(1.74 \pm 0.06) \times 10^{26}$  molecules s<sup>-1</sup> for  
4 8P, an improvement in the confidence limits of a factor of 3 (see Fig. 15) with respect to  
5 the previously reported value derived with the old ethane fluorescence model (see Table  
6 1 and Böhnhardt et al. [2008]).

7 A similar improvement was obtained with spectra of comet C/2004 Q2 (Machholz) (Q2  
8 hereafter), which was observed using NIRSPEC in November 2004 and January 2005  
9 [Bonev et al. 2009]. We applied the new C<sub>2</sub>H<sub>6</sub> model to the spectra taken on 19 January  
10 2005 [Fig. 13] and retrieved a production rate of  $(13.3 \pm 0.25) \times 10^{26}$  mol s<sup>-1</sup> at 93K (a  
11 correction of -12% to the value for T<sub>rot</sub> reported previously) with a confidence limit  
12 improved by a factor of 3. Considering a Q(H<sub>2</sub>O) of  $(2.727 \pm 0.070) \times 10^{29}$  mol s<sup>-1</sup> as  
13 reported by Bonev et al. [2009] for this date, this would correspond to an ethane mixing  
14 ratio of  $0.488 \pm 0.016$  %. This mixing ratio is consistent with that derived from the v<sub>5</sub>  
15 band of ethane for November 28 2004 by Radeva et al. [2011] of  $0.48 \pm 0.06$  %. Lastly,  
16 comet C/2007 W1 (Boattini) (W1 hereafter) was observed in July 2008 using NIRSPEC  
17 [Fig. 14]. The comet has a particularly rich chemistry, and the ethane Q-branches are  
18 very bright in our spectra. From the co-measured water spectrum and considering 20 lines  
19 of H<sub>2</sub>O, we retrieved a rotational temperature of  $79 \pm 3$  K for H<sub>2</sub>O on 9 July 2008 (see  
20 details in Villanueva et al., in prep.). The C<sub>2</sub>H<sub>6</sub> production rate for W1 at 79K is  $(2.35 \pm$   
21  $0.02) \times 10^{26}$  mol s<sup>-1</sup>. For the three comets, we measured E<sub>g</sub>/A<sub>g</sub> ratios to be consistent with  
22 equilibrium ( $T_{\text{spin}} > 10$ K).

1 As shown in Figs. 12, 13, 14 and 15, the new model shows excellent line-by-line  
2 agreement with the cometary datasets, ultimately allowing us to extract improved  
3 cometary abundances [see Table 2]. The new model also has led to improved  
4 understanding of this complex spectral region, where many other hydrocarbons have  
5 strong spectral signatures (e.g., methanol ( $\text{CH}_3\text{OH}$ ), methane ( $\text{CH}_4$ ) and ethylene ( $\text{C}_2\text{H}_4$ )).

6 The improvement of the  $\text{C}_2\text{H}_6$  fluorescence model is attributed to differences between the  
7 old [Dello-Russo et al. 2001] and new models arising from four aspects: 1) the previous  
8 model did not properly account for the symmetries of l-splitting of rotational levels of the  
9  $v_7$  vibrational level, leading to incorrect ro-vibrational branching ratios; 2) we introduced  
10 updated molecular constants, partition functions, and performed a line-by-line analysis  
11 (instead of a temperature independent “g-band” analysis); 3) we included the complete  
12 fine rotational structure (P, Q, and R-branches) of the  $v_7$  band (including hot-bands)  
13 leading to an overall increase in the considered flux integrated within each Q-branch; and  
14 4) the new model considers a realistic solar pumping spectrum.

15

## 16 **6. Conclusions**

17 We constructed a line-by-line model for the  $v_7$  band of ethane ( $\text{C}_2\text{H}_6$ ), and applied it to  
18 compute telluric transmittances, and cometary fluorescence efficiencies. The complex  
19 and dense rotational fine structure of the  $v_7$  band system was described using a set of  
20 accurate rotational constants for each K-ladder, including torsional hot-bands. The new  
21 band systems were integrated into an advanced radiative transfer model of the terrestrial  
22 atmosphere (LBLRTM), considering a rigorous line-by-line, layer-by-layer radiative

1 transfer analysis and including realistic atmospheric conditions, abundance profiles, and  
2 geometrical conditions. In addition to adding 17,266 ethane lines ( $\nu_7$  and  $\nu_7 + \nu_4 - \nu_4$ ) to  
3 the spectral database accessed by the terrestrial model, we updated and expanded the CO<sub>2</sub>  
4 database by including our latest discoveries in the Martian atmosphere. Using these new  
5 models, we achieved excellent agreement with transmittance and fluorescence emission  
6 data recorded near 3.3  $\mu\text{m}$  using three different instruments located in the Northern and  
7 Southern hemispheres.

8 We computed cometary fluorescence emission rates for a wide range of rotational  
9 temperatures (10-200K), and successfully validated the model by comparing it to  
10 measured spectra of three comets (C/2007 W1 (Boattini), C/2004 Q2 (Machholz) and  
11 8P/Tuttle). The model makes use of a novel approach to synthesize the solar pumping,  
12 which combines a theoretical continuum model and a highly precise solar line list. The  
13 methodology used to calculate cometary fluorescence emission rates was standardized to  
14 extract information from existing spectral databases on C<sub>2</sub>H<sub>6</sub> as well as all other  
15 molecules in the HITRAN database, and so is readily available to compute cometary  
16 fluorescence emission rates for multiple other molecules.

17

## 18 **Acknowledgements**

19 GLV acknowledges support from NASA's Planetary Astronomy Program (08-PAST08-  
20 0034) and NASA's Planetary Atmospheres Program (08-PATM08-0031). MJM was  
21 supported by NASA's Planetary Astronomy Program (RTOP 344-32-07) and NASA's  
22 Astrobiology Program (RTOP 344-53-51). KMS was supported by the Planetary

1 Astronomy RUI program of the National Science Foundation. We thank Dr. Hans-Ulrich  
2 Käufl for assisting with the Mars (CRIRES) observations in 2009, and Dr. Robert Novak  
3 and Dr. Avram M. Mandell for assisting with the acquisition of Mars (CSHELL) data in  
4 2006. We thank the staff of the VLT Observatory, (operated by ESO), of the W. M. Keck  
5 Observatory (operated as a scientific partnership among CalTech, UCLA, and NASA),  
6 and of NASA's InfraRed Telescope Facility (operated for NASA by the University of  
7 Hawaii) for their exceptional support throughout our long Mars and cometary observing  
8 Programs. The authors wish to recognize and acknowledge the very significant cultural  
9 role and reverence that the summit of Mauna Kea has always had within the indigenous  
10 Hawaiian community. We are most fortunate to have the opportunity to conduct  
11 observations from this mountain.

12

### 13 **References**

- 14 Abrams, M.C., Goldman, A., Gunson, M. R., Rinsland, C. P., Zander, R. (1996),  
15 Observations of the infrared solar spectrum from space by the ATMOS experiment,  
16 *Applied Optics*, vol. 35 pp. 2747.  
17  
18 Anderson, G.P., Clough, S.A., Kneizys, F.X., Chetwynd, J.H., and Shettle, E.P. (1986).  
19 AFGL Atmospheric Constituent Profiles (0-120 km), *AFGL-TR-86- 0110, Air Force*  
20 *Geophysics Laboratory*, Hanscom AFB MA, 43 pp.  
21  
22 Blass, W.E., Halsey G.W., Susskind J., Reuter D.C., Jennings D.E. (1990), Rotational  
23 parameters of the first torsional state of ethane from lower state combination differences  
24 in v9 + v4 - v4, *J. Mol. Spectrosc.*, vol. 141 pp. 334.  
25  
26 Böhnhardt, H., Mumma, M. J., Villanueva, G. L., DiSanti, M. A., Bonev, B. P., Lippi,  
27 M., Käufl, H. U. (2008), The Unusual Volatile Composition of the Halley-Type Comet  
28 8P/Tuttle: Addressing the Existence of an Inner Oort Cloud, *Astrophys. J.*, vol. 683 pp.  
29 L71.  
30  
31 Bonev, B. P., Mumma, M. J., Gibb, E. L., DiSanti, M. A., Villanueva, G. L., Magee-  
32 Sauer, K., Ellis, R. S. (2009), Comet C/2004 Q2 (Machholz): Parent Volatiles, a Search

- 1 for Deuterated Methane, and Constraint on the CH<sub>4</sub> Spin Temperature, *Astrophys. J.*, Vol.  
2 699 pp. 1563.
- 3
- 4 Brown, L. R., Farmer, C. B., Rinsland, C. P. and Toth, R. A. (1987), Molecular line  
5 parameters for the Atmospheric Trace Molecule Spectroscopy (ATMOS) Experiment, *Appl.*  
6 *Opt.*, Vol. 26, 5154 - 5182.
- 7
- 8 Clough, S.A., Shephard, M.W., Mlawer, E.J., Delamere, J.S., Iacono, M.J., Cady-Pereira,  
9 K., Boukabara, S., Brown, P.D. (2005), Atmospheric radiative transfer modeling: a  
10 summary of the AER codes, *J. Quant. Spectrosc. Radiat. Transfer*, vol. 91 pp. 233.
- 11
- 12 Cole, A. R. H., Cross, K. J., Cugley, J. A., Heise, H. M. (1980), Infrared rotation-  
13 vibration spectra of ethane . The perpendicular band v<sub>7</sub> of C<sub>2</sub>H<sub>6</sub>, *J. Mol. Spectrosc.*, Vol.  
14 83 pp. 233.
- 15
- 16 Crovisier, J., Encrenaz, T. (1983), Infrared fluorescence of molecules in comets - The  
17 general synthetic spectrum, *Astron. Astrophys.*, vol. 126 pp. 170.
- 18
- 19 Dang-Nhu, M., Pine, A.S., Lafferty, W.J. (1984), Intensities in the v<sub>5</sub>, v<sub>7</sub>, and v<sub>8</sub> + v<sub>11</sub>  
20 bands of ethane <sup>12</sup>C<sub>2</sub>H<sub>6</sub>, *Can. J. Phys.*, vol. 62 pp. 512.
- 21
- 22 Dang-Nhu, M., Goldman, A. (1987), Line parameters for C<sub>2</sub>H<sub>6</sub> in the 3000 cm<sup>-1</sup> region, *J.*  
23 *Quant. Spectrosc. Radiat. Transfer*, Vol. 38 pp. 159.
- 24
- 25 Dello Russo, N. D., Mumma, M. J., DiSanti, M. A., Magee-Sauer, K., Novak, R. (2001),  
26 Ethane Production and Release in Comet C/1995 O1 Hale-Bopp, *Icarus*, 153, pp 162.
- 27
- 28 Dello Russo, N. D., Mumma, M. J., DiSanti M. A., Magee-Sauer, K., Gibb, E. L., Bonev,  
29 B.P., McLean, I. S., Xu, L. (2006), A high-resolution infrared spectral survey of Comet  
30 C/1999 H1 Lee, *Icarus*, vol. 184 pp. 255.
- 31
- 32 DiSanti, M.A., Mumma, M.J. (2008), Reservoirs for Comets: Compositional Differences  
33 Based on Infrared Observations, *Space Sci. Rev.*, vol. 138 pp. 127.
- 34
- 35 Edwards, D. P. (1992), GENLN2: A general line-by-line atmospheric transmittance and  
36 radiance model, Version 3.0 description and users guide, NCAR/TN-367-STR, *National*  
37 *Center for Atmospheric Research*, Boulder, Co.
- 38
- 39 Gamache, R. R., Hawkins, R. L., Rothman, L. S. (1990), Total internal partition sums in  
40 the temperature range 70-3000 K: Atmospheric linear molecules, *J. Mol. Spectrosc.*, vol.  
41 142 pp. 205.
- 42
- 43 Glatthor, N., von Clarmann, T., Stiller, G.P., Funke, B., Koukouli, M.E., Fischer, H.,  
44 Grabowski, U., Höpfner, M., Kellmann, S., Linden, A. (2009), Large-scale upper  
45 tropospheric pollution observed by MIPAS HCN and C<sub>2</sub>H<sub>6</sub> global distributions, *Atmos.*  
46 *Chem. Phys.*, vol. 9 pp. 9619.
- 47

- 1 Goldman, A., Dang-Nhu, M., Bouanich J. P. (1989), Ethane 3  $\mu\text{m}$  spectral clusters of  
2 atmospheric interest, *J. Quant. Spectrosc. Radiat. Transfer*, Vol. 41 pp. 17.
- 3
- 4 Goldman, A., Gamache, R. R., Perrin, A., Flaud, J. M., Rinsland, C. P., Rothman, L. S.  
5 (2000), HITRAN partition function and weighted transition-moments squared, *J. Quant.*  
6 *Spectrosc. Radiat. Transfer*, Vol 66, 455–86.
- 7
- 8 Fernández, J.M., Montero, S. (2003), Torsional selection rules, Raman tensors, and cross  
9 sections for degenerate modes of  $\text{C}_2\text{H}_6$ , *J. Chem. Phys.*, vol. 118 pp. 2657.
- 10
- 11 Fiorenza C., Formisano V. (2005), A solar spectrum for PFS data analysis, *Planet. Space*  
12 *Sci.*, Vol. 53 pp. 1009.
- 13
- 14 Fischer J., Gamache R. R., Goldman A., Rothman L. S., Perrin A. (2003), Total internal  
15 partitions sums for molecular species on the 2000 edition of the HITRAN database, *J.*  
16 *Quant. Spectrosc. Radiat. Transfer*, Vol 82, 401–12.
- 17
- 18 Harrison, J.J., Allen, N.D.C, Bernath, P.F. (2010), Infrared absorption cross sections for  
19 ethane ( $\text{C}_2\text{H}_6$ ) in the 3  $\mu\text{m}$  region, *J. Quant. Spectrosc. Radiat. Transfer*, vol. 111 pp. 357.
- 20
- 21 Hase, F., Demoulin, P., Sauval, A. J., Toon, G. C., Bernath, P. F., Goldman, A.,  
22 Hannigan, J. W., Rinsland, C. P. (2006), An empirical line-by-line model for the infrared  
23 solar transmittance spectrum from 700 to 5000  $\text{cm}^{-1}$ , *J. Quant. Spectrosc. Radiat.*  
24 *Transfer*, vol. 102 pp. 450.
- 25
- 26 Hase, F., Wallace, L., Mcleod, S. D., Harrison, J. J., Bernath, P. F. (2010), The ACE-FTS  
27 atlas of the infrared solar spectrum, *J. Quant. Spectrosc. Radiat. Transfer*, Vol. 111 (4)  
28 pp. 521-528.
- 29
- 30 Helmig, D., Bottenheim, J., Galbally, I. E., Lewis, A., Milton, M. J. T., Penkett, S., Plass-  
31 Duelmer, C., Reimann, S., Tans, P., Thiel, S. (2009), Volatile Organic Compounds in the  
32 Global Atmosphere, *Eos Trans. Am. Geophys. Union*, vol. 90 pp. 513.
- 33
- 34 Herzberg, G. (1945), Molecular Spectra and Molecular Structure: II. Infrared and Raman  
35 Spectra of Polyatomic Molecules, *Van Nostrand Inc.*, Princeton, New Jersey.
- 36
- 37 Hough, A. M. (1991), Development of a Two-Dimensional Global Tropospheric Model:  
38 Model Chemistry, *J. Geophys. Res.*, 96(D4), 7325–7362.
- 39
- 40 Käufl, H., et al. (2004), CRIRES: a high-resolution infrared spectrograph for ESO's VLT.  
41 Ground-based Instrumentation for Astronomy. Edited by Alan F. M. Moorwood and Iye  
42 Masanori, *Proc. SPIE Int. Soc. Opt. Eng.*, vol. 5492 pp. 1218.
- 43
- 44 Kunde, V.R., Maguire, W.C. (1974). Direct integration transmittance model, *J. Quant.*  
45 *Spectrosc. Radiat. Transfer*, vol. 14 pp. 803.
- 46

- 1 Kurucz R. L. (1997), The solar irradiance by computation. <http://kurucz.harvard.edu/>.
- 2
- 3 Malathy Devi, V., Benner, D.C., Rinsland, C.P., Smith, M.A.H., Sams, R.L., Blake, T.A.,  
4 Flaud, J., Sung, K., Brown, L.R., Mantz, A.W. (2010a), Multispectrum measurements of  
5 spectral line parameters including temperature dependences of N<sub>2</sub>- and self-broadened  
6 half-width coefficients in the region of the v<sub>9</sub> band of <sup>12</sup>C<sub>2</sub>H<sub>6</sub>, *J. Quant. Spectrosc. Radiat.*  
7 *Transfer*, vol. 111 pp. 2481.
- 8
- 9 Malathy Devi, V., Rinsland, C.P., Benner C.D., Sams, R.L., Blake, T.A. (2010b),  
10 Multispectrum analysis of the v<sub>9</sub> band of <sup>12</sup>C<sub>2</sub>H<sub>6</sub>: Positions, intensities, self- and N<sub>2</sub>-  
11 broadened half-width coefficients, *J. Quant. Spectrosc. Radiat. Transfer*, vol. 111 pp.  
12 1234.
- 13
- 14 McLean, I.S., et al. (1998), Design and development of NIRSPEC: a near-infrared echelle  
15 spectrograph for the Keck II telescope, *Proc. SPIE Int. Soc. Opt. Eng.*, Vol. 3354, pp.  
16 566.
- 17
- 18 Mumma, M. J., DiSanti, M. A., Dello Russo, N. D., Fomenkova, M., Magee-Sauer, K.,  
19 Kaminski, C.D., Xie, D.X. (1996), Detection of Abundant Ethane and Methane, Along  
20 with Carbon Monoxide and Water, in Comet C/1996 B2 Hyakutake: Evidence for  
21 Interstellar Origin, *Science*, vol. 272 pp. 1310.
- 22
- 23 Mumma, M. J. et al. (2001), A Survey of Organic Volatile Species in Comet C/1999 H1  
24 (Lee) Using NIRSPEC at the Keck Observatory, *Astrophys. J.*, vol. 546 pp. 1183.
- 25
- 26 Mumma, M.J., Charnley, S. B. (2011), Annu. Rev. Astron. Astr., under review.
- 27
- 28 Oomens, J., Reuss, J. (1996), The v<sub>7</sub>+ v<sub>9</sub>- v<sub>9</sub> Hot Band in Ethane, *J. Mol. Spectrosc.*, vol.  
29 177 pp. 19.
- 30
- 31 Pine, A. S., Lafferty, W. J. (1982), Torsional Splittings and Assignments of the Doppler-  
32 Limited Spectrum of Ethane in the C-H Stretching Region, *J. Res. Nat. Bur. Stand.*, vol.  
33 83 (3) pp. 1-20.
- 34
- 35 Pine, A. S., Rinsland, C. P. (1999), The role of torsional hot bands in modeling  
36 atmospheric ethane, *J. Quant. Spectrosc. Radiat. Transfer*, vol. 62 pp. 445.
- 37
- 38 Pine, A. S., Stone, S. C. (1996), Torsional Tunneling and A<sub>1</sub>-A<sub>2</sub> Splittings and Air  
39 Broadening of the <sup>R</sup>Q<sub>0</sub> and <sup>P</sup>Q<sub>3</sub> Subbranches of the v<sub>7</sub> Band of Ethane, *J. Mol. Spectrosc.*,  
40 vol. 175 pp. 21.
- 41
- 42 Radeva, Y.L., Mumma, M. J., Villanueva, G. L., A'Hearn, M. F. (2011), A Newly  
43 Developed Fluorescence Model for C<sub>2</sub>H<sub>6</sub> v<sub>5</sub> and Application to Cometary Spectra  
44 Acquired with NIRSPEC at Keck II, *Astrophys. J.*, vol. 729 (2) pp. 135.
- 45

- 1 Rinsland, C.P., Goldman, A., Murcray, F.J., David, S.J., Blatherwick, R.D., Murcray,  
2 D.G. (1994), Infrared spectroscopic measurements of the ethane ( $C_2H_6$ ) total column  
3 abundance above Mauna Loa, Hawaii - seasonal variations, *J. Quant. Spectrosc. Radiat.*  
4 *Transfer*, vol. 52 pp. 273.  
5
- 6 Rinsland, C.P., Jones, N.B., Connor, B.J., Wood, S.W., Goldman, A., Stephen, T.M.,  
7 Murcray, F.J., Chiou, L.S., Zander, R., Mahieu, E. (2002), Multiyear infrared solar  
8 spectroscopic measurements of HCN, CO,  $C_2H_6$ , and  $C_2H_2$  tropospheric columns above  
9 Lauder, New Zealand (45°S latitude), *J. Geophys. Res. Atmos.*, vol. 107 pp. 4185.  
10
- 11 Rothman, L.S., et al. (2009), The HITRAN 2008 molecular spectroscopic database, *J.*  
12 *Quant. Spectrosc. Radiat. Transfer*, vol. 110 pp. 533.  
13
- 14 Rothman, L. S., Hawkins, R. L., Wattson, R. B., Gamache, R. R. (1992), Energy levels,  
15 intensities, and linewidths of atmospheric carbon dioxide bands, *J. Quant. Spectrosc.*  
16 *Radiat. Transfer*, vol. 48 pp. 537.  
17
- 18 Šimečková, M., Jacquemart, D., Rothman, L.S., Gamache, R.R., Goldman, A. (2006),  
19 Einstein A-coefficients and statistical weights for molecular absorption transitions in the  
20 HITRAN database, *J. Quant. Spectrosc. Radiat. Transfer*, Vol. 98 pp. 130.  
21
- 22 Snodgrass, H.B., Ulrich R.K (1990), Rotation of Doppler features in the solar  
23 photosphere, *Astrophys. J.*, vol. 351 pp. 309.  
24
- 25 Tobiska, W.K., Woods, T., Eparvier, F., Viereck, R., Floyd, L., Bouwer, D., Rottman, G.,  
26 White, O.R. (2000), The SOLAR2000 empirical solar irradiance model and forecast tool,  
27 *J. Atmos. Sol. Terr. Phys.*, 62, pp. 1233–1250  
28
- 29 Tokunaga, A.T., Toomey, D.W., Carr, J., Hall, D.N.B., Epps, H.W. (1990), Design for a  
30 1-5 micron cryogenic Echelle spectrograph for the NASA IRTF, *Instrumentation in*  
31 *astronomy VII; Proceedings of the Meeting*, vol. 1235 pp. 131.  
32
- 33 Vandaele, A.C, Villanueva, G. L., Bertaux, J. L., Borkov, Y., Drummond, R., Mahieux,  
34 A., Montmessin, F., Mumma, M. J., Novak, R. E., Perevalov, V., Tashkun, S., Wilquet,  
35 V. (2009), Updating  $CO_2$  spectroscopic line list using Mars and Venus spectra,  
36 International Conference on Comparative Planetology: Venus – Earth – Mars, *European*  
37 *Space Agency, ESTEC*, Noordwijk, The Netherlands, 11- 15 May.  
38
- 39 Villanueva, G. L., Mumma, M. J., Novak, R. E., Hewagama, T. (2008a), Identification of  
40 a new band system of isotopic  $CO_2$  near 3.3  $\mu m$ : Implications for remote sensing of  
41 biomarker gases on Mars, *Icarus*, vol. 195 pp. 34.  
42
- 43 Villanueva, G. L., Mumma, M. J., Novak, R. E., Hewagama, T. (2008b), Discovery of  
44 multiple bands of isotopic  $CO_2$  in the prime spectral regions used when searching for  $CH_4$   
45 and HDO on Mars, *J. Quant. Spectrosc. Radiat. Transfer*, vol. 109 pp. 883.  
46

1 Wallace, L., Livingston, W. (2003), An Atlas of the Solar Spectrum in the Infrared from  
2 1850 to (1.1 to 5.4 microns), *revised*. N.S.O. Technical Report #03-001, National Solar  
3 Observatory, Tucson.

4

5 Weaver, H.A., Mumma, M.J. (1984), Infrared molecular emissions from comets,  
6 *Astrophys. J.*, Vol. 276 pp. 782.

7

8

<b>Rotational constants for the ground state (Pine &amp; Lafferty 1982)</b>								
		$A_0 = 2.671$	$B_0 = 0.6630271$	$D_0^K = 1.09 \times 10^{-5}$				
		$D_0^{JK} = 2.660 \times 10^{-6}$	$D_0^J = 1.0312 \times 10^{-6}$					
<b>Rotational constants for the <math>v_7</math> vibrational state<sup>(a)</sup></b>								
$K\ell'$	Sym	F [cm $^{-1}$ ]	B [cm $^{-1}$ ]	$D \times 10^{-6}$ [cm $^{-1}$ ]	Lines	r.m.s. [cm $^{-1}$ ]		
-8	A <sub>s</sub>	3120.55085	0.66367616	1.6379	6	0.00083		
-8	E <sub>s</sub>	3120.57306	0.66354001	1.0500	4	0.00781		
-7	E <sub>u</sub>	3089.50468	0.66330074	0.7167	15	0.00749		
-6	E <sub>u</sub>	3062.67031	0.66214093	-2.0388	22	0.00632		
-5	A <sub>s</sub>	3039.18324	0.66383076	17.2659	19	0.00750		
-5	E <sub>s</sub>	3039.36507	0.66090799	-4.2371	10	0.00103		
-4	E <sub>u</sub>	3020.45860	0.66348953	2.1859	25	0.00699		
-3	E <sub>s</sub>	3005.61858	0.66348639	1.7780	11	0.01241		
-3	G <sub>s</sub>	3005.63978	0.66329109	1.2006	23	0.00344		
-2	A <sub>s</sub>	2994.84157	0.66312225	0.9459	14	0.00002		
-2	E <sub>s</sub>	2994.83990	0.66312201	0.9767	10	0.00005		
-1	E <sub>u</sub>	2988.09979	0.66303157	0.8945	36	0.00124		
0	E <sub>u</sub> <sup>(b)</sup>	2985.38894	0.66303542	1.0141	22	0.00155		
1	A <sub>u</sub> <sup>(b)</sup>	2986.72474	0.66308908	1.0296	31	0.00245		
1	A <sub>s</sub> <sup>(c)</sup>	2986.72634	0.66289178	0.9789	14	0.00002		
1	E <sub>s</sub> <sup>(c)</sup>	2986.73272	0.66285832	1.1544	10	0.00004		
2	E <sub>s</sub>	2992.09430	0.66299073	1.2681	15	0.00241		
2	G <sub>s</sub>	2992.09721	0.66292818	1.0268	32	0.00644		
3	E <sub>s</sub>	3001.50382	0.66315921	1.4885	27	0.00776		
3	G <sub>s</sub>	3001.50571	0.66294774	0.9871	26	0.00428		
4	A <sub>s</sub>	3014.94266	0.66295652	0.9703	32	0.00111		
4	E <sub>s</sub>	3014.93730	0.66296202	1.0594	16	0.00047		
5	E <sub>u</sub>	3032.40473	0.66300958	0.8346	34	0.00127		
6	E <sub>u</sub>	3053.85189	0.66352169	0.6270	53	0.00565		
7	A <sub>u</sub>	3079.69389	0.65843003	-4.3470	41	0.00808		
8	E <sub>s</sub>	3108.98384	0.66162133	0.5372	19	0.00072		
8	G <sub>s</sub>	3108.98763	0.66150373	0.4632	38	0.00748		
9	E <sub>u</sub>	3142.50886	0.66190851	0.8715	16	0.00164		
10	A <sub>s</sub>	3180.03893	0.66210580	1.3212	22	0.00133		
10	E <sub>s</sub>	3180.03545	0.66215115	1.3664	11	0.00185		

1

<b>Perturbation coefficients and high order rotational constants<sup>(a)</sup></b>					
<b>K<math>\ell'</math></b>	<b>Sym</b>	<b>P<sub>1</sub></b>	<b>P<sub>2</sub></b>	<b>P<sub>3</sub></b>	<b>H x 10<sup>-11</sup> [cm<sup>-1</sup>]</b>
-7	E <sub>u</sub>	0.1760	9.6954	-1.3818	
-6	E <sub>u</sub>				-240.7280
-4	E <sub>u</sub>	2.8068	21.2584	-1.7843	338.1293
-3	G <sub>s</sub>	0.2090	5.9299	-0.9862	
1	A <sub>s</sub>				5.2861 <sup>(c)</sup>
1	E <sub>s</sub>				51.1299 <sup>(c)</sup>
2	G <sub>s</sub>	0.4384	23.9358	-1.0348	
3	E <sub>s</sub>	0.3688	11.2986	-1.9035	
3	G <sub>s</sub>	0.3524	13.5662	-1.7339	
7	A <sub>u</sub>	0.0367	15.4387	-0.1476	-253.0972
8	G <sub>s</sub>	0.3183	20.7249	-1.3233	
10	A <sub>s</sub>	0.0430	16.4071	-1.3051	
10	E <sub>s</sub>	0.1812	17.6675	-0.9935	
<b>Rotational constants for the -8 &gt; K &gt; 10<sup>(d)</sup></b>					
$v_0 = 2985.3953$ $B' = 0.66311490$ $A_{\zeta}' = 0.34385599$					
$A'-B' = 2.0208281$ $D_j' = 8.9352 \times 10^{-7}$ $D_{JK}' = 6.8549 \times 10^{-6}$					
$D_K' = -2.0192 \times 10^{-5}$ $n_j' = -7.82 \times 10^{-5}$ $nK' = -7.12 \times 10^{-4}$					
<b>Intensity factors for the <math>v_7</math> band of ethane</b>					
$S_v^0(296K) = 301(24) [\text{cm}^{-2} \text{ atm}^{-1}] = 1.21(10) \times 10^{-17} [\text{cm}^{-1}/(\text{molecule cm}^{-2})]$					
$\alpha = 0.0096(20)$ $\beta = -0.0034(20)$ $Q_R(296K) = 51617$					
<b>Lineshape parameters for K beyond those reported in Malathy Devi et al. [2010a,b]<sup>(e)</sup></b>					
$n_1$ (N <sub>2</sub> temperature dependence): $A = 0.6756$ $B = 0.0112$ ( $J_0=0$ )					
$n_2$ (SELF temperature dependence): $A = 0.5687$ $B = 0.0085$ ( $J_0=0$ )					
$b_L^0(N_2)$ width: $a_0 = 0.1011$ $a_1 = -1.3352 \times 10^{-3}$ $a_2 = 1.9690 \times 10^{-5}$					
$b_L^0$ (SELF) width: $b_0 = 0.1401$ $b_1 = -1.6279 \times 10^{-3}$ $b_2 = 2.3211 \times 10^{-5}$					

2

3

4 **Table 1:** Spectroscopic constants for the  $v_7$  band of ethane. (a) Rotational constants and  
5 perturbations were obtained for each K-ladder considering equations 2 and 3. (b) For  ${}^RQ_0$ ,  
6 limitations in the description of the ground-state were circumvented by defining a  
7 different set of upper-state rotational constants for  $\Delta J \neq 0$ . (c) Rotational constants for the  
8  ${}^RQ_0$  ( $\Delta J=0$ ) branch were obtained from Pine and Stone 1996. (d) For high K sub-bands,  
9 we fitted the energies of all lines (with the exception of the highly perturbed  $K''=4,5,6$ ) to  
10 the global progression presented in equations 4 and 5. (e) For lines accessing  $K''$  higher  
11 than those available in Malathy Devi et al. [2010a,b], we considered the mean  
12 progressions as presented in Figure 4.

13

1  
2

Level	$\ell$	K	J	D <sub>3d</sub> notation	G <sup>+</sup> <sub>36</sub> notation
Ground (A <sub>1g</sub> )	0	0	0,2,4	A <sub>1g</sub> (8)	A <sub>1s</sub> (6) + E <sub>3s</sub> (2)
			1,3,5	A <sub>2g</sub> (16)	A <sub>2s</sub> (10) + E <sub>4s</sub> (6)
		1,2,4,5	All	E <sub>g</sub> (20)	E <sub>1s</sub> (4) + G <sub>s</sub> (16)
		3,6,9		A <sub>1g</sub> (8)+A <sub>2g</sub> (16)	A <sub>1s</sub> (6) + E <sub>3s</sub> (2) + A <sub>2s</sub> (10) + E <sub>4s</sub> (6)
	$v_7$ (E <sub>u</sub> )	-1		E <sub>u</sub> (20)	E <sub>2s</sub> (4) + G <sub>s</sub> (16)
		0,1,3,4,6,7		A <sub>1u</sub> (8)+A <sub>2u</sub> (16)	A <sub>3s</sub> (6) + E <sub>3s</sub> (2) + A <sub>4s</sub> (10) + E <sub>4s</sub> (6)
		2,5,8		E <sub>u</sub> (20)	E <sub>2s</sub> (4) + G <sub>s</sub> (16)
		0,2,3,5,6,8		A <sub>1u</sub> (8)+A <sub>2u</sub> (16)	A <sub>3s</sub> (6) + E <sub>3s</sub> (2) + A <sub>4s</sub> (10) + E <sub>4s</sub> (6)
		1,4,7			

3  
4  
5  
6  
7  
8

**Table 2:** Symmetries of the rotational levels of the ground and  $v_7$  vibrational states considering the D<sub>3d</sub> and G<sup>+</sup><sub>36</sub> point groups. The G<sup>+</sup><sub>36</sub> permutation-inversion group is used when internal torsional tunneling is considered. Statistical weights for each spin species are presented in brackets.

1

ID	Frequency [cm <sup>-1</sup> <sup>(a)</sup>	E <sub>rot</sub> [cm <sup>-1</sup> ]	g-factor <sup>(c)</sup> x 10 <sup>-5</sup> [s <sup>-1</sup> ]	Trans.	TOA Flux <sup>(b)</sup> x 10 <sup>-18</sup> [W m <sup>-2</sup> ]	Production rate x 10 <sup>26</sup> [s <sup>-1</sup> ]
<b>Comet C/2007 W1 (Boattini) – Trot = 79K</b>						<b>2.3513</b>
<sup>R</sup> Q <sub>4</sub>	3000.2124	90.81	<b>1.58545</b>	0.8666	1.0369	0.0250
<sup>R</sup> Q <sub>2</sub>	2993.4586	73.30	<b>2.55965</b>	0.9100	1.6418	0.0244
<sup>R</sup> Q <sub>1</sub>	2990.0776	63.13	<b>3.07130</b>	0.8132	2.0151	0.0256
<sup>R</sup> Q <sub>0</sub>	2986.7182	56.56	<b>3.97371</b>	0.9453	2.6096	0.0204
<sup>P</sup> Q <sub>1</sub>	2983.3840	58.10	<b>3.06727</b>	0.9581	1.9262	0.0212
<sup>P</sup> Q <sub>2</sub>	2980.0774	67.43	<b>2.58050</b>	0.7873	1.7046	0.0267
<sup>P</sup> Q <sub>3</sub>	2976.7854	81.82	<b>2.19640</b>	0.9491	1.4041	0.0242
<b>Comet C/2004 Q2 (Machholz) – Trot = 93K</b>						<b>13.309</b>
<sup>R</sup> Q <sub>4</sub>	3000.2230	108.50	<b>1.62755</b>	0.8664	4.0881	0.0623
<sup>R</sup> Q <sub>2</sub>	2993.4579	84.47	<b>2.44481</b>	0.7769	6.1209	0.0719
<sup>R</sup> Q <sub>1</sub>	2990.0752	75.42	<b>2.85883</b>	0.7882	7.4671	0.0604
<sup>R</sup> Q <sub>0</sub>	2986.7144	69.13	<b>3.65410</b>	0.8820	10.148	0.0643
<sup>P</sup> Q <sub>1</sub>	2983.3840	69.34	<b>2.84345</b>	0.8796	7.1421	0.0498
<sup>P</sup> Q <sub>2</sub>	2980.0768	78.37	<b>2.45732</b>	0.7311	6.3405	0.1423
<sup>P</sup> Q <sub>3</sub>	2976.7883	93.62	<b>2.18030</b>	0.9213	5.3157	0.0585
<b>Comet 8P/Tuttle – Trot = 60K</b>						<b>1.7383</b>
<sup>R</sup> Q <sub>4</sub>	3000.2855	100.18	<b>0.95049</b>	0.9095	0.2265	0.0406
<sup>R</sup> Q <sub>1</sub>	2990.0819	49.10	<b>3.29522</b>	0.7555	0.8215	0.0686
<sup>R</sup> Q <sub>0</sub>	2986.7192	42.09	<b>4.48408</b>	0.8769	1.1869	0.0468
<sup>P</sup> Q <sub>1</sub>	2983.3820	44.73	<b>3.36980</b>	0.9115	0.7589	0.0425
<sup>P</sup> Q <sub>2</sub>	2980.0731	51.61	<b>2.69160</b>	0.7414	0.6785	0.0624

2

**Table 3:** IDs, frequencies ( $\nu$ ), weighted rotational energies ( $E_{\text{rot}}$ ), TOA g-factors (g) at  $R_h=1\text{AU}$ , transmittances, TOA measured fluxes and production rates (Q) for 7 Q sub-branches of the  $\nu_7$  band of  $\text{C}_2\text{H}_6$ . a) The rest-frequency is the weighted mean of the frequencies composing each Q-branch, where the weight is the g-factor x transmittance for each compounding line. b) Total transmittance-corrected flux considering a  $0.432 \times 1.782 \text{ arcsec}^2$  box for the W1 and Q2 results (NIRSPEC) and  $0.400 \times 1.29 \text{ arcsec}^2$  for the 8P results (CRIRES). c) Integrated fluorescence efficiencies in the spectral region of the corresponding Q-branch from the new model synthesized with the appropriate rotational temperatures and heliocentric velocities – 8P/Tuttle:  $T_{\text{rot}} = 60 \text{ K}$  and  $v_h = -0.37 \text{ km s}^{-1}$ , C/2007 W1:  $T_{\text{rot}} = 79 \text{ K}$  and  $v_h = +9.70 \text{ km s}^{-1}$ , C/2004 Q2:  $T_{\text{rot}} = 93 \text{ K}$  and  $v_h = -2.01 \text{ km s}^{-1}$ .

14

1

Atmosphere	1. Abundance relative to std. profile	2. Ethane ( $C_2H_6$ ) Mixing ratios
<b>Mars – Ethane (<math>C_2H_6</math>) search <sup>(a)</sup></b>		
62°N-62°S, 295-308°W at $L_s=323^\circ$ (MY 29), 18 August 2009		< 0.8 ppb (3 $\sigma$ )
41°N-76°S, 57-67°W at $L_s=352^\circ$ (MY 27), 6 January 2006		< 1.5 ppb (3 $\sigma$ )
<b>Earth – Ethane (<math>C_2H_6</math>) surface level volume mixing ratio <sup>(b)</sup></b>		
Mauna Kea (4,200 m, Hawaii), 6 Jan 2006	<b>0.49 ± 0.03</b>	(0.97 ± 0.06) ppb
Paranal (2,635 m, Chile), 18 August 2009	<b>0.15 ± 0.02</b>	(0.30 ± 0.04) ppb
<b>Comets - Ethane (<math>C_2H_6</math>) abundance relative to water (<math>H_2O</math>) <sup>(c)</sup></b>		
C/2007 W1 (Boattini), 9 July 2008, NIRSPEC at Keck II		(1.957 ± 0.053) %
C/2004 Q2 (Machholz), 19 January 2005, NIRSPEC at Keck II		(0.488 ± 0.016) %
8P/Tuttle, 26 January 2008, CRIRES at VLT		(0.291 ± 0.017) %

2

3

**Table 4:** Measured ethane abundance in selected planetary and cometary atmospheres. **a)** Mars: We searched for ethane at 7 latitudinal intervals along the central meridian in August 2009 and January 2006, achieving extremely high sensitivities. The spectra presented in Figs. 4 and 5 also sample the methane P-branch, allowing us to obtain in Jan 2006 a sensitive upper limit for  $CH_4$  of < 8 ppb [3 $\sigma$ ] (consistent with Mumma et al. 2009). The data taken with CRIRES in August 2009 were test exposures and the Doppler-shift (-9.4 km s<sup>-1</sup>) was not sufficient to search for  $CH_4$  on Mars. **b)** Assuming the “standard” Northern hemisphere vertical profile as presented in Fig 3c, we retrieved the scaling factor presented in column ‘1’. A value of 0.15 (1/7) is consistent with the findings of Helmig et al. 2009 for the Southern Hemisphere. Mixing ratios at surface level on site are presented in column ‘2’. The value for Mauna Kea is similar to the findings of Rinsland et al. [1994] for Mauna Loa at this season (corrected for hot-band absorption, see text). **c)** The ethane mixing ratios in comets are defined with respect to water, the main volatile constituent.

17

18

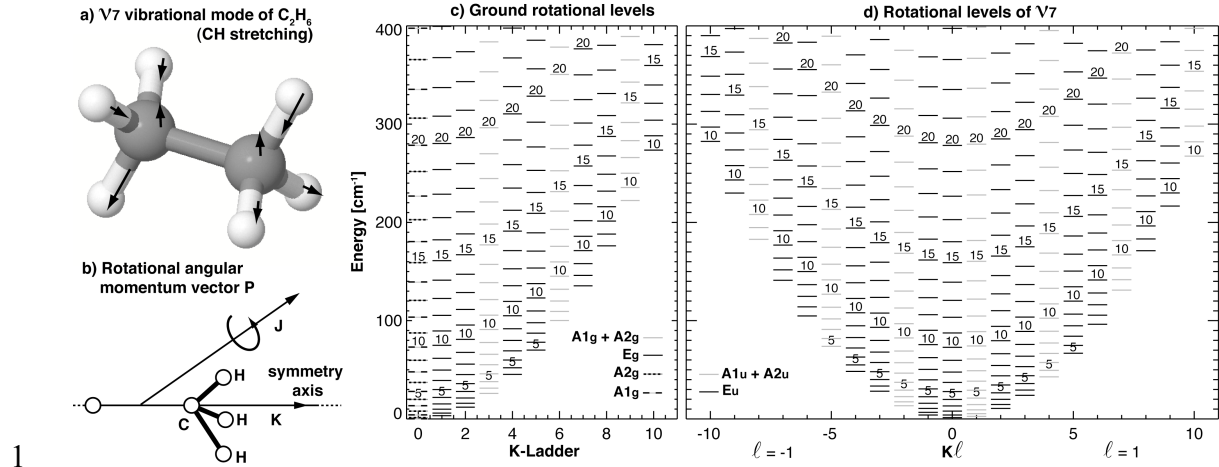


**Figure 1.** Rotational structure of the ground and  $\nu_7$  vibrational levels of  $\text{C}_2\text{H}_6$ . Panel ‘a’ shows the relative motions of the atoms of  $\text{C}_2\text{H}_6$  associated with the  $\nu_7$  vibrational mode. Panel ‘b’ shows the rotational angular momentum (related to the  $J$  quantum number), and its projection along the symmetry-axis (related to the  $K$  quantum number). Panels ‘c’ and ‘d’ show rotational levels for the ground and  $\nu_7$  vibrational states, respectively, with symmetries indicated by different trace types.

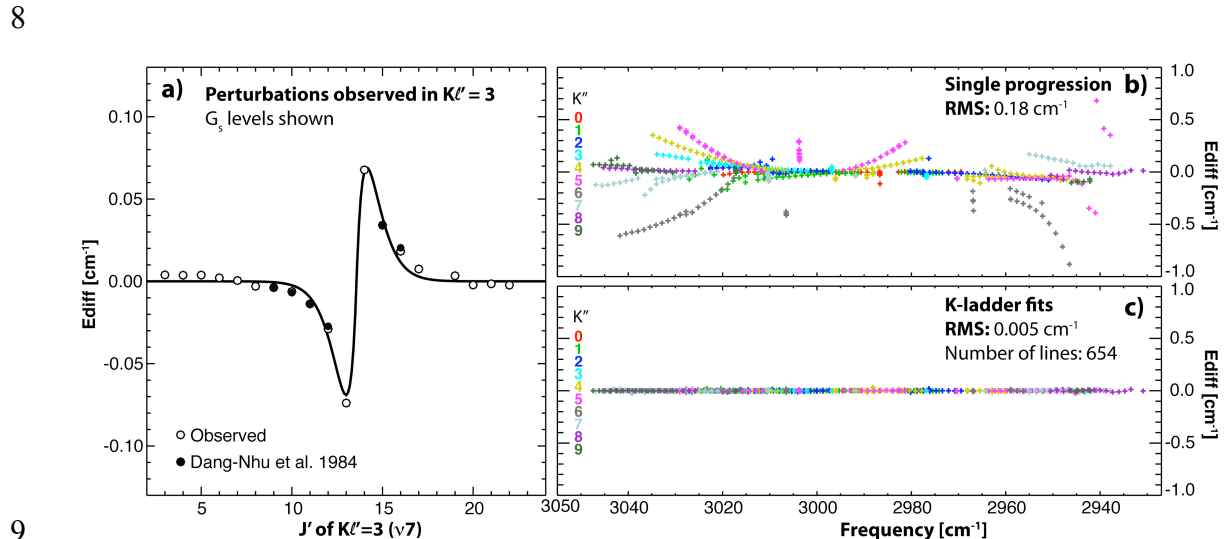
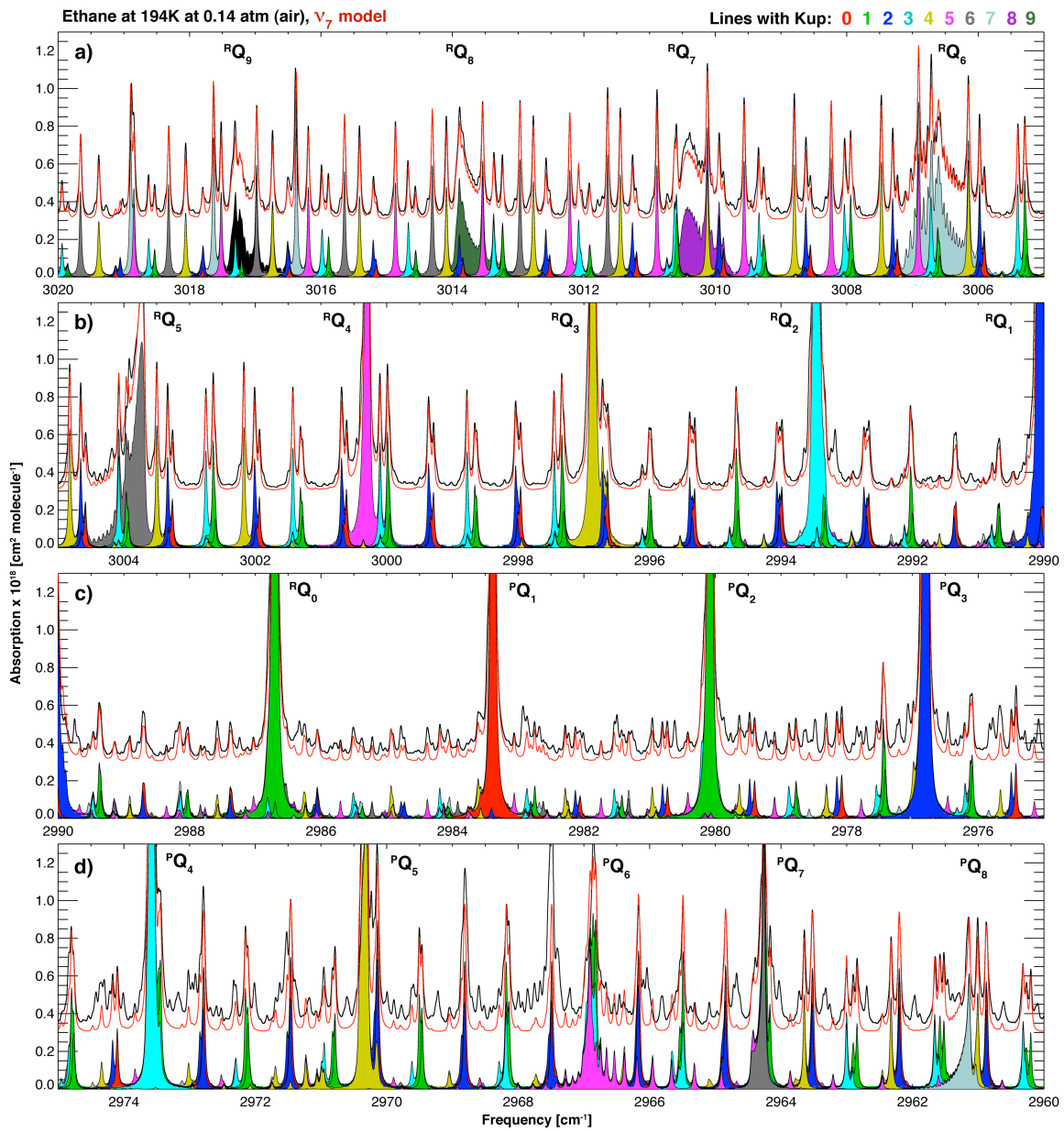


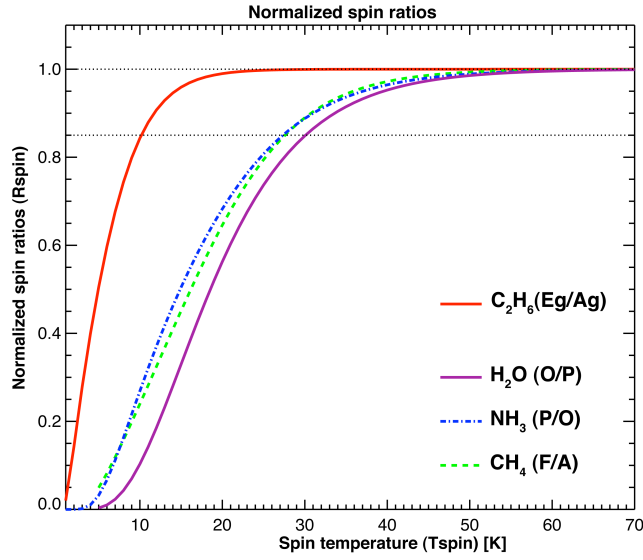
**Figure 2:** Description of the rotational levels of the  $\nu_7$  vibrational state. Panel ‘a’ shows the effect of local perturbations on the energy distribution of the rotational levels. The empirical values were fitted to a quadratic progression and a perturbation function (trace) considering the values presented in Table 1. Panel ‘b’ shows the energy residuals obtained when performing a global fit to the rotational lines of the  $\nu_7$  vibrational level using a single progression for all  $K$ -ladders. Panel ‘c’ shows the residuals for 654 lines using individual coefficients for each  $K$ -ladder (see Table 1).



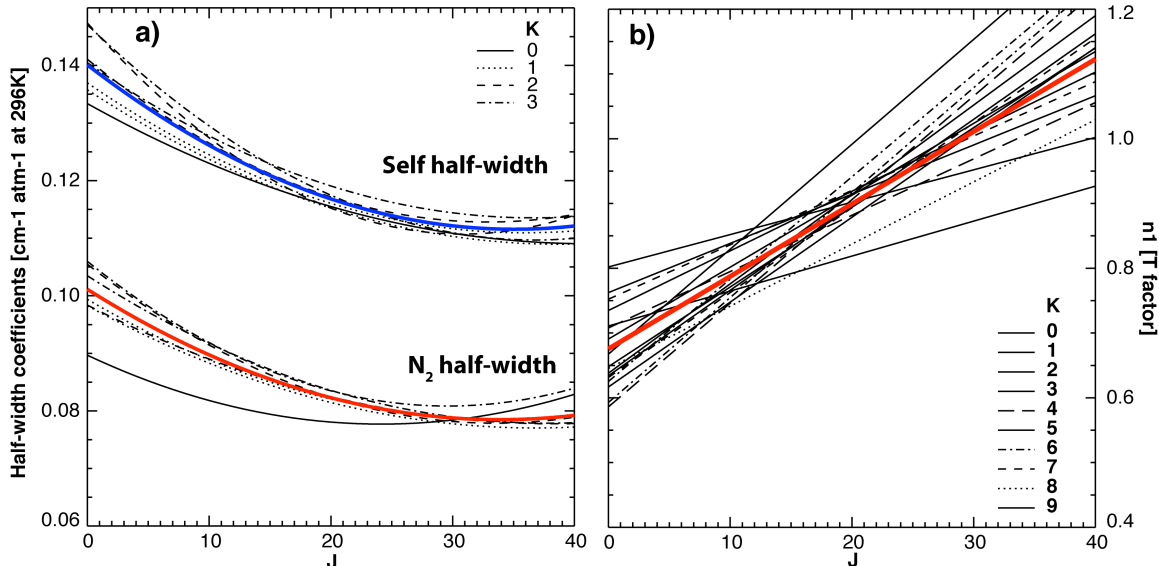
1

2 **Figure 3:** Individual K sub-bands of the  $\nu_7$  band of ethane compared to absorption cross  
 3 sections obtained by Harrison et al. [2010] for a temperature of 194K and a pressure of  
 4 0.14 atm of synthetic air. The total model (red) and measured (black trace) absorption  
 5 cross sections have been displaced by 0.3 for clarity purposes.

6



1  
2 **Figure 4:** Symmetry ratio of ethane ( $A_g = A_{1g} + A_{2g}$  and  $E_g$  considering the  $D_{3d}$  point  
3 group,  $E_g/A_g=5/3$  at equilibrium) in comparison to water ( $\text{H}_2\text{O}$ , O/P=3 at eq.), ammonia  
4 ( $\text{NH}_3$ , P/O=1 at eq.) and methane ( $\text{CH}_4$ , F/A=9/5 at eq.).  
5



6  
7 **Figure 5:** Lineshape parameters progressions retrieved by Malathy Devi et al. [2010a,b]  
8 for the  $v_9$  band of ethane and applied to our model of the  $v_7$  band. For  $K$  values with no  
9 available measurements we computed a weighted mean progression, shown in the figure  
10 with a thick color trace. The coefficients of the weighted mean progressions are presented  
11 in Table 1.  
12  
13

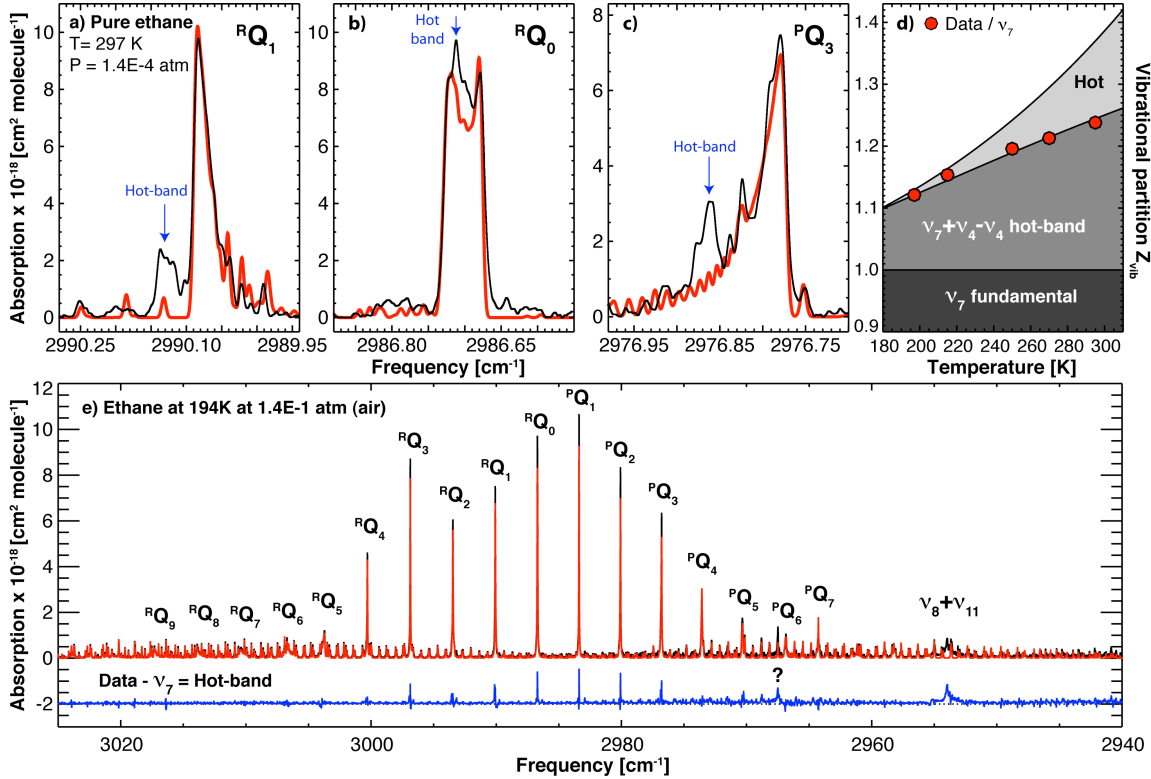
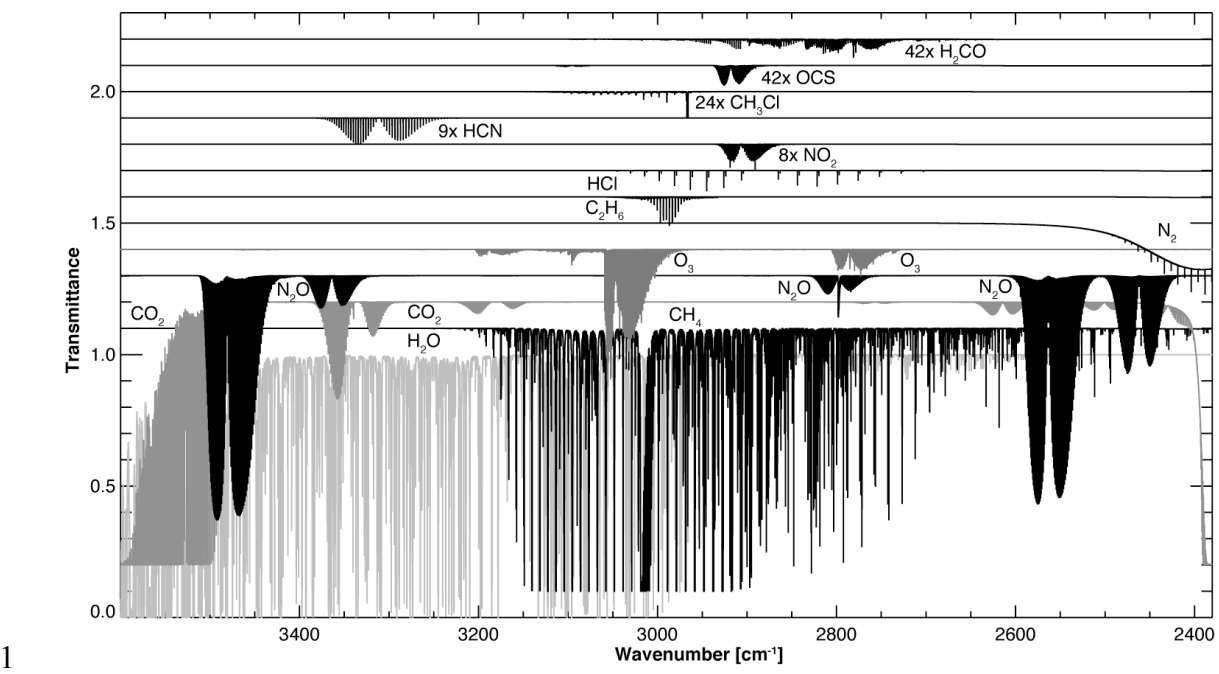


**Figure 6:** Identification of the  $v_7$  hot-band of ethane. Panels ‘a’, ‘b’ and ‘c’ show comparisons of model spectra with pure ethane spectra recorded by Harrison et al. [2010] at 297K and  $1.4 \times 10^{-4}$  atmospheres. At these low pressures, the fine structure of the Q-branches is nicely revealed, showing unaccounted absorptions that we associate with the first torsional hot-band of the  $v_7$  band. Panel ‘d’ shows the ratio of the area of the strongest Q-branches ( $K'' \leq 4$ , with the exception of  ${}^PQ_1$ , see text) with respect to the modeled  $v_7$  absorption, integrated around  $(\pm 0.3 \text{ cm}^{-1})$  at each K-band center. The fact that the ratio coincides with the vibrational partition function of the  $v_7$  level and its first torsional component suggests that these absorptions are related to the  $v_7 + v_4 - v_4$  hot-band.

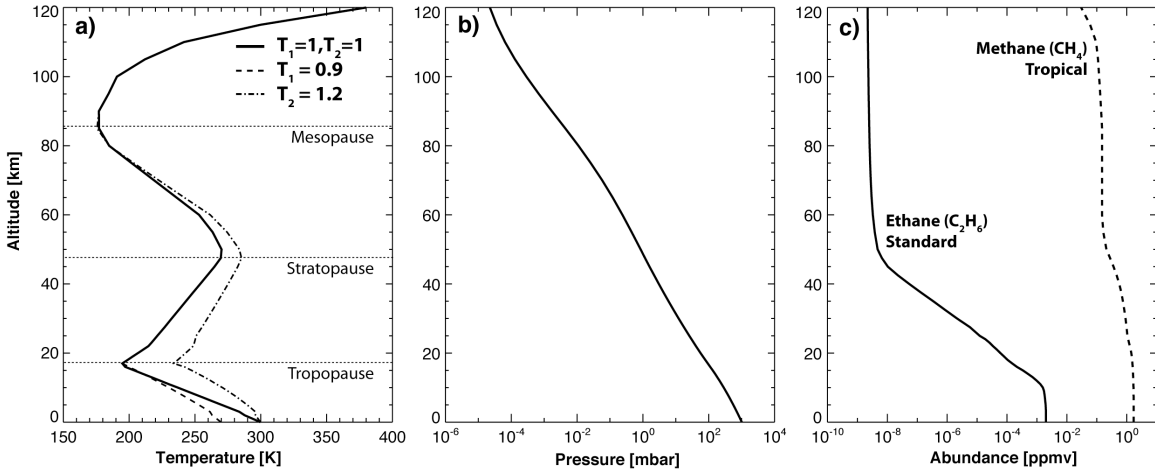
11

12

13



2 **Figure 7.** Representative terrestrial spectra synthesized with the LBLRTM line-by-line  
 3 and layer-by-layer radiative transfer model, and utilizing our updated spectral database.  
 4 The spectra were synthesized for airmass 1.0 (zenith), and (adopted) nominal  
 5 abundances, temperatures and pressures for Mauna Kea at 4,200 m altitude.  
 6



2 **Figure 8.** Vertical profiles of temperature (a), pressure (b), and mixing ratios for  $\text{CH}_4$  and  
 3  $\text{C}_2\text{H}_6$  (c) adopted for synthesizing terrestrial spectra. The temperature profile ‘a’ is  
 4 organized into tropospheric (affected by  $T_1$ ) and stratospheric (affected by  $T_2$ ) sectors,  
 5 while the pressure profile (Panel ‘b’) is the standard tropical pressure profile scaled with  
 6 a multiplier (see text). Temperatures and pressures are scaled relative to the standard  
 7 tropical value (Anderson et al. 1986).

8  
 9

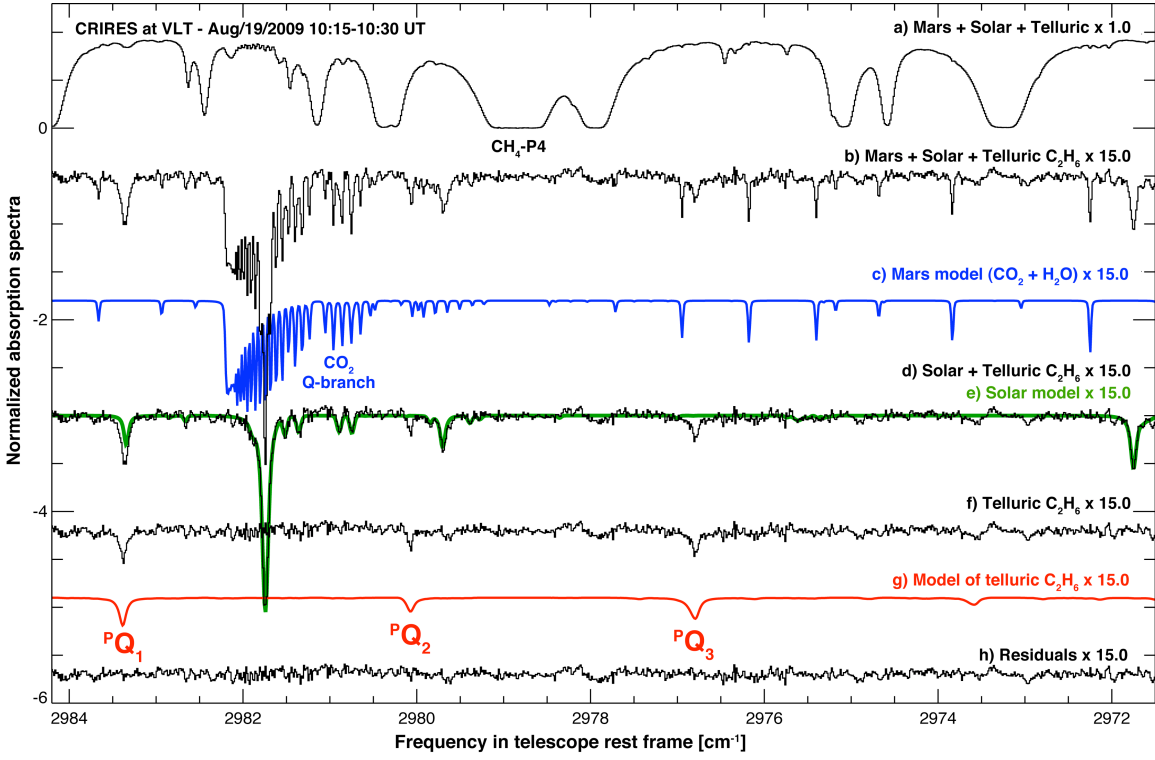
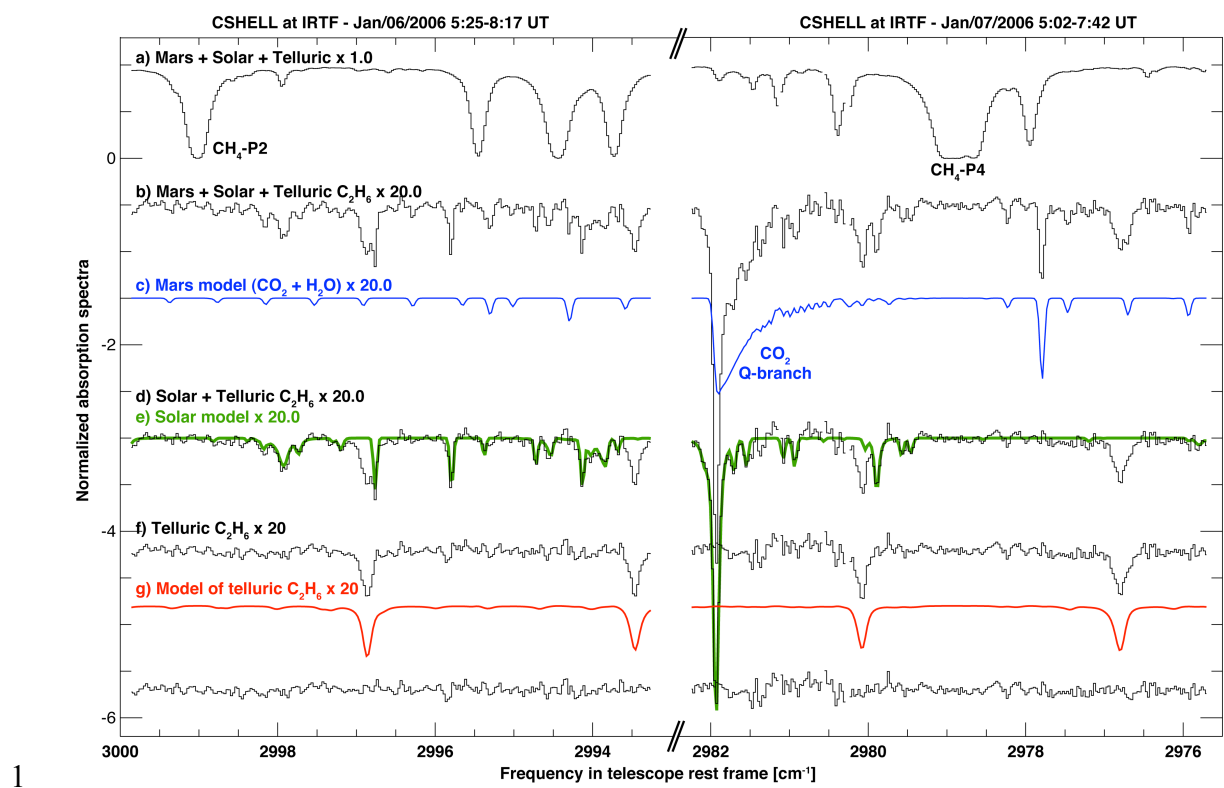


**Figure 9.** Mars infrared spectrum taken on 18 August 2009 with CRIRES at VLT (total of 8 minutes integration time on source). Trace ‘a’ shows the calibrated Mars continuum affected by terrestrial transmittance, and trace ‘b’ shows the Mars residual spectrum after removing a terrestrial model (with no  $\text{C}_2\text{H}_6$ ). Trace ‘d’ shows the residual spectrum after removing a Martian absorption spectrum containing  $\text{CO}_2$  and  $\text{H}_2\text{O}$  (trace ‘c’). Trace ‘d’ shows the residual spectrum containing solar Fraunhofer lines and telluric  $\text{C}_2\text{H}_6$  lines, while trace ‘e’ is a model of the solar spectrum considering the new method presented in Appendix B. Trace ‘f’ shows the residual telluric ethane spectrum, and trace ‘h’ shows the overall residual after removing a terrestrial spectrum synthesized with the new  $\text{C}_2\text{H}_6$   $\nu_7$  band model (trace ‘g’).

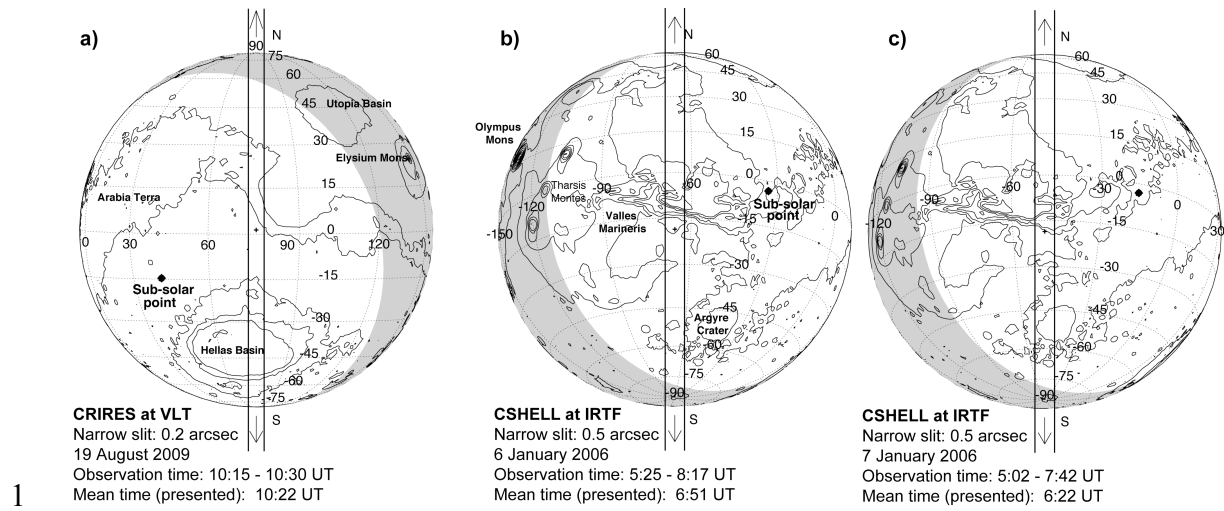
12

13



2 **Figure 10.** Mars infrared spectra taken on 6-7 January 2006 using two CSHELL-IRTF  
 3 settings (the total integration time on source was 40 (52) minutes for the left (right)  
 4 spectrum). See Figure 4 for a description of the traces. The spectral sharpness of the  
 5 spectral features is higher in Figure 4 because of higher resolving power ( $\lambda/\Delta\lambda \sim 90,000$ )  
 6 with CRIRES (for CSHELL,  $\lambda/\Delta\lambda \sim 40,000$ ). The terrestrial  $C_2H_6$  lines appear stronger in  
 7 the Northern hemisphere (compare Southern Hemisphere, Figure 4) because of the higher  
 8 abundance of volatile organic compounds (VOCs, including  $C_2H_6$ ) that arise mainly from  
 9 biogenic and anthropogenic emissions.

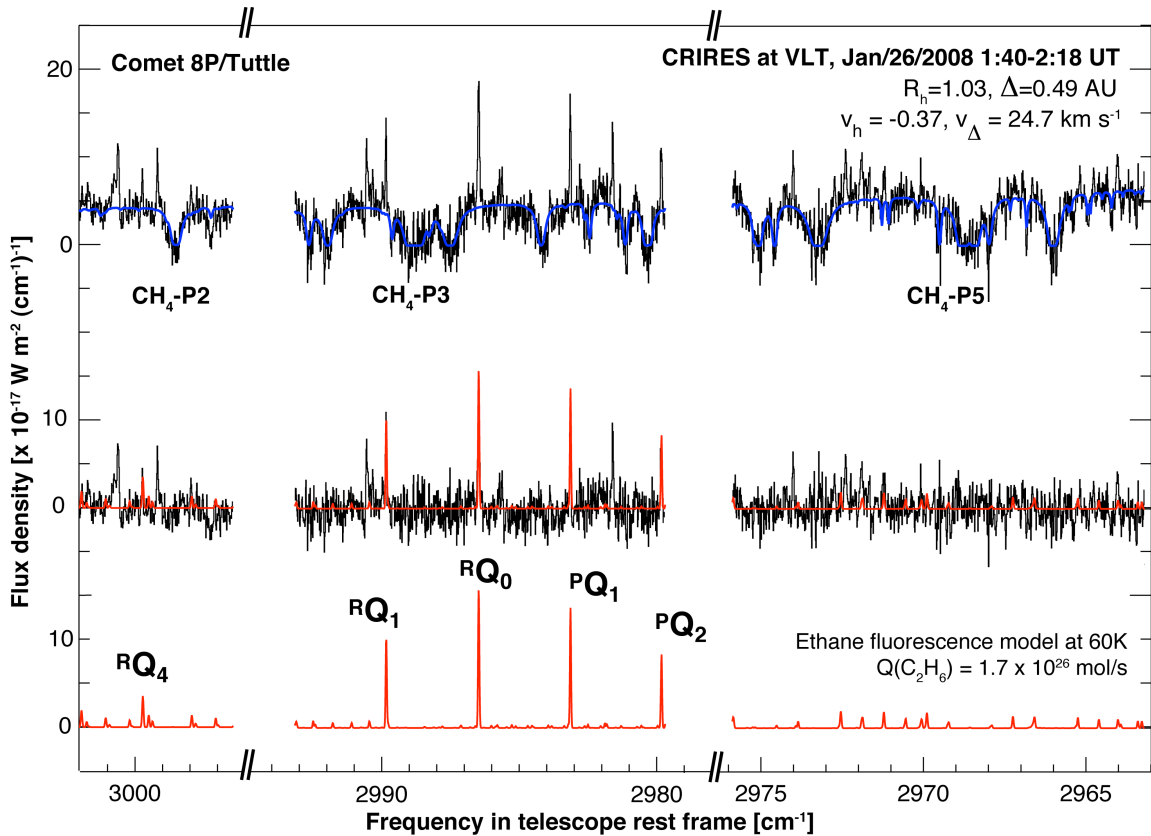
10



2 **Figure 11.** Geometry diagrams presenting the orientation of the spectrometer's entrance  
 3 slit for CRIRES data taken on 19 August 2009 (a), and CSHELL data taken on 6-7  
 4 January 2006 (b and c panels). We used the narrowest slit for each instrument (0.2" for  
 5 CRIRES, 0.5" for CSHELL), and oriented the slit North-South on the planet for the three  
 6 measurements.

7

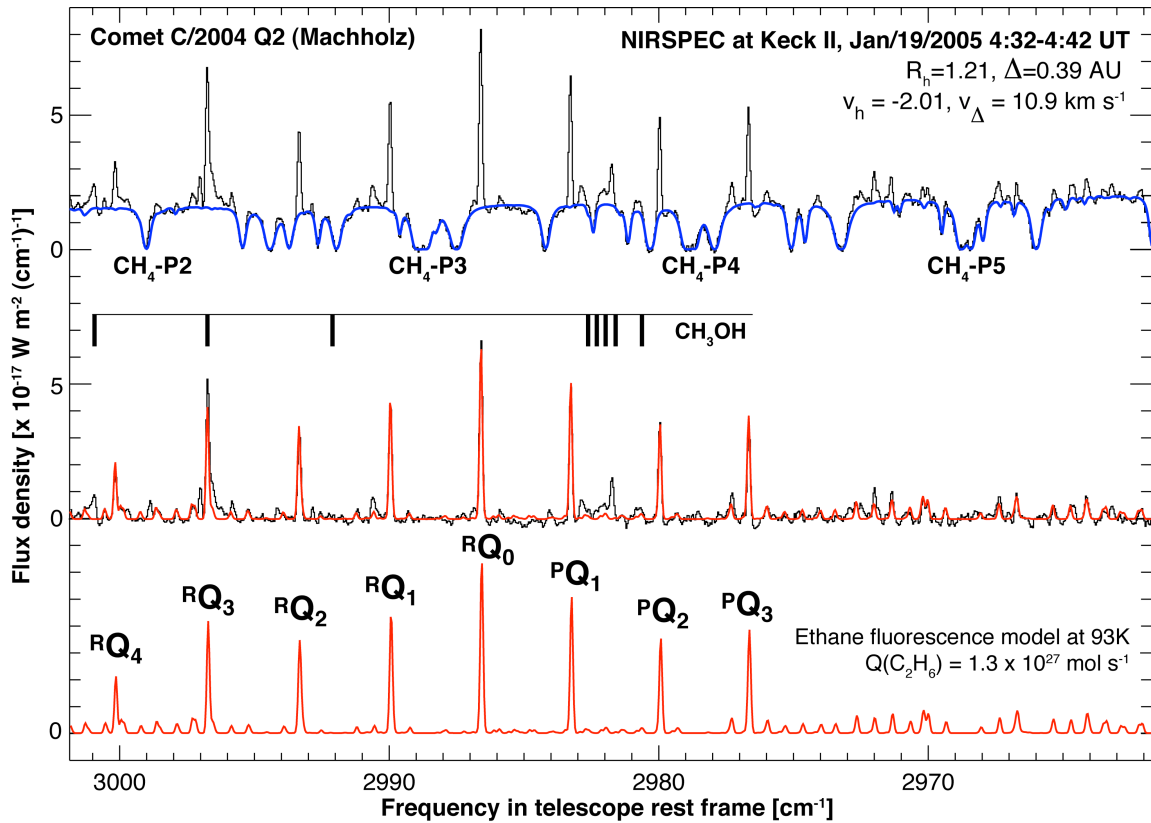
8



1

2 **Figure 12.** Infrared spectrum of comet 8P/Tuttle taken on 26 January 2008 using  
3 CRIRES at VLT (Böhnhardt et al. 2008). The upper trace shows a spectrum extracted  
4 from the sum of 15 spatial rows centered on the comet nucleus, and a continuum model  
5 affected by terrestrial transmittance is overlaid. The mid-trace (residual spectrum) reveals  
6 lines of the  $\nu_7$  band of C<sub>2</sub>H<sub>6</sub> in emission (with model overlaid).

7



1

2 **Figure 13.** Infrared spectrum of comet C/2004 Q2 (Machholz) taken on 19 January 2005  
 3 using NIRSPEC at Keck II (Bonev et al. 2009). The upper trace shows the measured  
 4 spectrum extracted from the sum of 9 spatial rows centered on the comet nucleus, and a  
 5 continuum model affected by terrestrial transmittance is overlaid. The mid-trace shows  
 6 the emission residual that reveals the  $\nu_7$  band of  $\text{C}_2\text{H}_6$  (with model overlaid) and certain  
 7  $\text{CH}_3\text{OH}$  lines.

8  
9

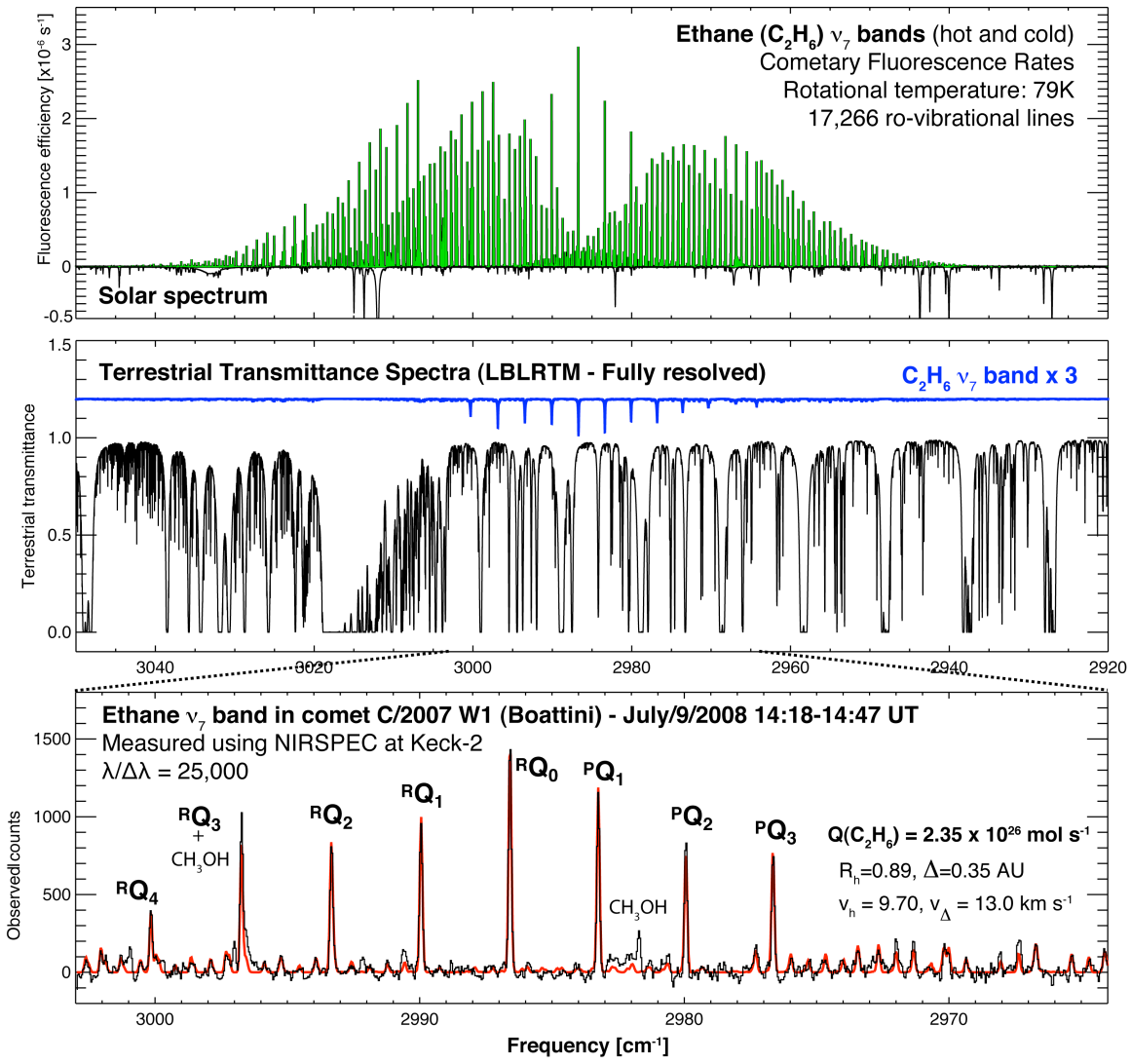


**Figure 14.** Fluorescence model of the  $\nu_7$  bands of  $\text{C}_2\text{H}_6$  and comparison with spectra of comet C/2007 W1 (Boattini) taken on 10 July 2008 with NIRSPEC at Keck II. **Upper-panel:** ethane fluorescence emission rates (g-factors) for 49366 lines of  $\nu_7$  (fundamental band) and  $\nu_7+\nu_4-\nu_4$  (hot-band) with  $T_{\text{rot}} = 79 \text{ K}$ ,  $v_h = +9.70 \text{ km s}^{-1}$  and  $R_h=1\text{AU}$ . **Mid-panel:** terrestrial transmittance and telluric  $\text{C}_2\text{H}_6$  absorption synthesized using LBLRTM. **Lower-panel:** High-resolution spectrum of comet Boattini showing the fine structure of the  $\nu_7$  band of  $\text{C}_2\text{H}_6$  (with model overlaid) and certain CH<sub>3</sub>OH lines.

9  
10

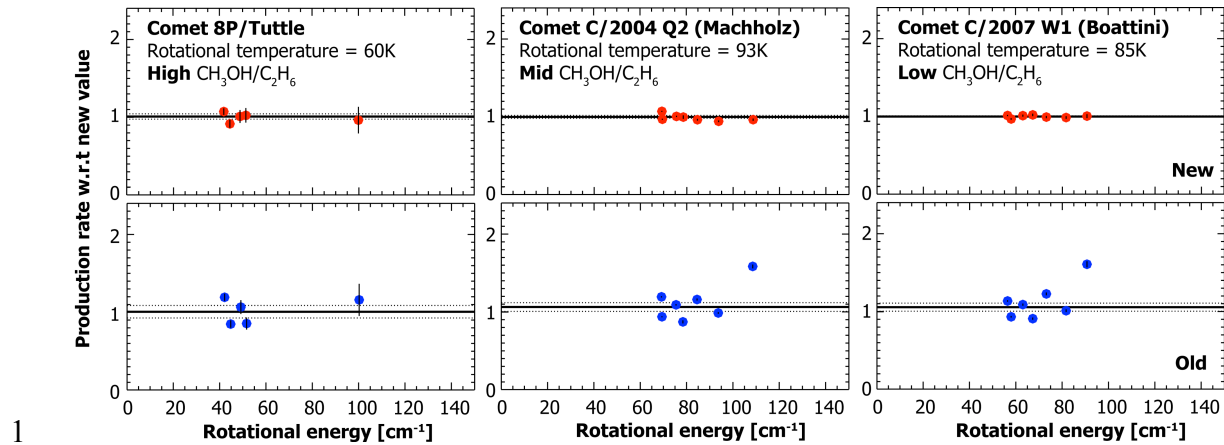


**Figure 15.** Excitation diagrams showing total production rates retrieved from individual ethane Q sub-branches, based on the new and old models (see details in Table 1). Results considering the new model are shown relative to the “new” mean in the upper panels, while the “old” results are presented in the lower panels.

6  
7

1    **Appendix A: HITRAN corrections and updates**

2    We use the universally recognized HITRAN database as the base for our radiative  
3    transfer model (using LBLRTM) and include our own corrections and updates. To the  
4    HITRAN 2008 release: 1) we applied the current updates available on the HITRAN  
5    website (<http://www.cfa.harvard.edu/hitran/updates.html>); 2) we added our new model  
6    for the  $\nu_7$  and  $\nu_7 + \nu_4 - \nu_4$  bands of C<sub>2</sub>H<sub>6</sub> (17,266 spectral lines); and 3) we expanded the  
7    CO<sub>2</sub> database to include our latest discoveries in the Martian atmosphere (1780 lines of 4  
8    bands, see below).

9    We recently discovered multiple unknown isotopic bands of CO<sub>2</sub> not previously  
10   described in the refereed literature (and not present in the HITRAN atlas), when  
11   analyzing spectra of CO<sub>2</sub>-rich Mars [Villanueva et al. 2008a,b]. The observations were  
12   performed using high-resolution echelle spectrometers, allowing us to extract precise  
13   spectroscopic constants for the levels involved (see Table 1 of Villanueva et al. [2008b]  
14   for the  $\nu_2 + \nu_3$  band of <sup>16</sup>O<sup>12</sup>C<sup>18</sup>O at 3.3 μm, the 2ν<sub>1</sub> band of <sup>16</sup>O<sup>12</sup>C<sup>17</sup>O at 3.6 μm, and the  
15   2ν<sub>1</sub> band of the rare isotope <sup>16</sup>O<sup>13</sup>C<sup>18</sup>O at 3.7 μm). In a follow-up study by the Venus  
16   Express SOIR Team, our detection of 2ν<sub>1</sub> (<sup>16</sup>O<sup>13</sup>C<sup>18</sup>O) band was confirmed and they have  
17   recently retrieved an improved set of spectroscopic constants for this band [Vandaele et  
18   al. 2009]. A compilation of all constants is presented in Table A-1.

19

20

21

1

Level	$G_v$ [cm <sup>-1</sup> ]	$B_v$ [cm <sup>-1</sup> ]	$D_v$ [cm <sup>-1</sup> ] x10 <sup>-7</sup>	$H_v$ [cm <sup>-1</sup> ] x10 <sup>-13</sup>	$S_v^0$ [cm <sup>-1</sup> / mol cm <sup>-2</sup> ] x10 <sup>-25</sup>	a1
<b><sup>16</sup>O<sup>12</sup>C<sup>18</sup>O (CO<sub>2</sub> 628)</b> – Villanueva et al. 2008a, Rothman et al. 1992						
00001	0.0	0.36818450	1.18647	-0.150		
<b>01111e</b>	<b>2982.11105</b>	0.36573112	1.20268	0.217	<b>1.83</b>	<b>-0.003</b>
<b>01111f</b>		<b>0.36626757</b>	<b>1.20380*</b>	<b>-0.296*</b>		
<b><sup>16</sup>O<sup>12</sup>C<sup>17</sup>O (CO<sub>2</sub> 627)</b> – Villanueva et al. 2008b, Rothman et al. 1992						
00001	0.0	0.37861462	1.26428	0.000		
<b>20001</b>	<b>2775.58690</b>	<b>0.37931621</b>	<b>1.48387</b>	<b>0.000</b>	<b>2.14</b>	
<b><sup>16</sup>O<sup>13</sup>C<sup>18</sup>O (CO<sub>2</sub> 638)</b> – Villanueva et al. 2008b, Vandaele et al. 2009, Rothman et al. 1992						
00001	0.0	0.36818116	1.18498	0.000		
<b>20001</b>	<b>2701.932484</b>	<b>0.36833043</b>	<b>0.872951</b>	<b>0.000</b>	<b>0.53</b>	

2

3 **Table A-1.** Carbon dioxide (CO<sub>2</sub>) ro-vibrational constants and band strengths. The band  
4 strengths are for transitions from the ground level and for an excitation temperature of  
5 296K. The value ‘a1’ is the first Herman-Wallis coefficient (Eq. 14 in Rothman et al.  
6 1992).

7

8

1    **Appendix B: Solar Spectrum**

2    We created a high-resolution flux-calibrated solar spectrum by combining an empirical  
3    line-by-line model for the infrared solar transmittance [Hase et al. 2006] with a purely  
4    theoretical model for the solar continuum irradiance [Kurucz 1997]; see Fig. B-1.  
5    Knowledge of the solar spectrum has greatly improved in the last few decades, due to  
6    spacecraft measurements (ATMOS mission [Abrams et al. 1996], ACE instrument [Hase  
7    et al. 2010]), and the comprehensive solar survey performed at the McMath-Pierce  
8    telescope at the Kitt-Peak National Observatory [Wallace and Livingston 2003]. These  
9    measurements integrated light from the entire Solar disk, and thus include factors such as  
10   limb darkening and other effects. One of the biggest limitations of these databases is that  
11   they are not flux calibrated, and the spectra can only be used to extract transmittance  
12   information. On the other hand, theoretical models have been extremely successful in  
13   calculating a flux-calibrated solar continuum, but their prediction of solar spectral  
14   features is still not optimum. There are several theoretical solar models (e.g. [Tobiska et  
15   al. 2000]). The Kurucz [1997] solar irradiance spectrum is considered best when  
16   averaged to [nm] resolutions [Fiorenza and Formisano 2005], but it does not describe the  
17   spectral morphology precisely (See Fig. B-2). In the case of the flux-calibrated solar  
18   spectrum presented in Fiorenza and Formisano [2005], we could not reproduce their  
19   reported values and we observe an error in the reported fluxes of a factor of  $\sim$ 15,000,  
20   introduced perhaps by an incorrect labeling of their flux units.

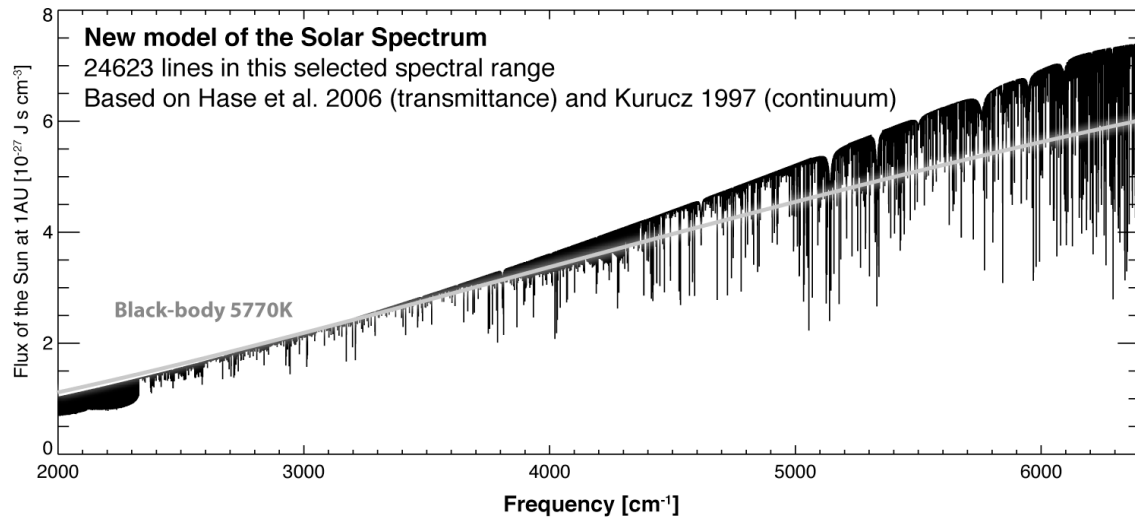
21   Using the ATMOS spectrum and other ground-based measurements of the Sun, Hase et  
22   al. [2006] generated an empirical line-by-line list model of the solar transmittance

1 spectrum. Recently, the same group has constructed a highly sensitive infrared solar  
2 spectrum from ACE-FTS observations [Hase et al. 2010] and they were able to assign  
3 numerous weak absorption features (that were not detectable in the ATMOS solar  
4 observations) due to the improved signal-to-noise of the ACE-FTS data. However, Hase  
5 et al. [2010] did not create line-by-line empirical data, only solar transmittance as a  
6 function of frequency.

7 The solar line list of Hase et al. [2006] includes intensities and identifications for each  
8 line and a parameterization of the lineshape (Gaussian w=0, Lorentzian w=1). It also  
9 accounts for center-to-limb variation of lines and continuum brightness temperature. In  
10 addition, the synthetic spectrum generated in this manner has a much greater signal-to-  
11 noise ratio, since each line can be properly described by just 4 line parameters. By  
12 multiplying this realistic transmittance spectrum of Hase et al. [2006] with the highly  
13 accurate continuum model of Kurucz [1997], we generated a flux-calibrated solar  
14 spectrum in the wavelength range 700-6400 cm<sup>-1</sup> (see Fig. 7). We simulate the integrated  
15 disk-spectrum by convolving the synthetic spectra with a solar rotation line-profile,  
16 which includes differential rotation (A:14.713 deg/day, B:-2.396 deg/day, C: -1.787  
17 deg/day; Snodgrass and Ulrich, 1990), limb darkening ( $u=0.6$ ) and the capability to  
18 compute integrated disk spectra for different inclinations (see Fig. B-3). At the ecliptic  
19 the broadening by this effect is  $\sim 2.5$  km s<sup>-1</sup> (FWHM). This approximation is far from  
20 optimum, but it provides an intermediate solution until a line-list for the integrated-disk at  
21 different inclinations becomes available. This spectrum was used to compute the  
22 fluorescence pumping in Eq. C-3. In Figure B-2 we show a comparison between the  
23 spacecraft solar spectrum measured by the ATMOS instrument [Abrams et al. 1996], the

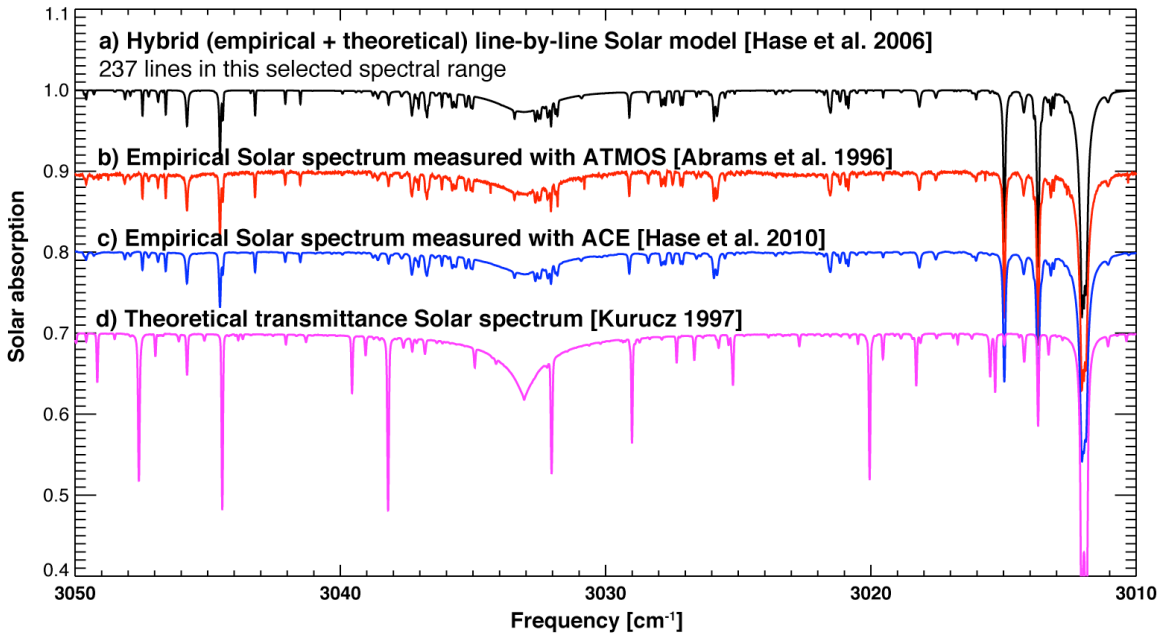
1 empirical line-by-line solar model using ATMOS data [Hase et al. 2006], the solar  
2 spectrum of Hase et al. [2010] using ACE-FTS data, and the theoretical solar irradiance  
3 spectrum by Kurucz [1997].

4



5  
6 **Figure B-1.** Spectrum of the Sun in the near-infrared region (1.6 to 5  $\mu\text{m}$ ) based on a  
7 theoretical model for the continuum [Kurucz 1997] and a new solar line list [Hase et al.  
8 2006]. The grey trace shows the continuum of a black body at 5770 K.  
9

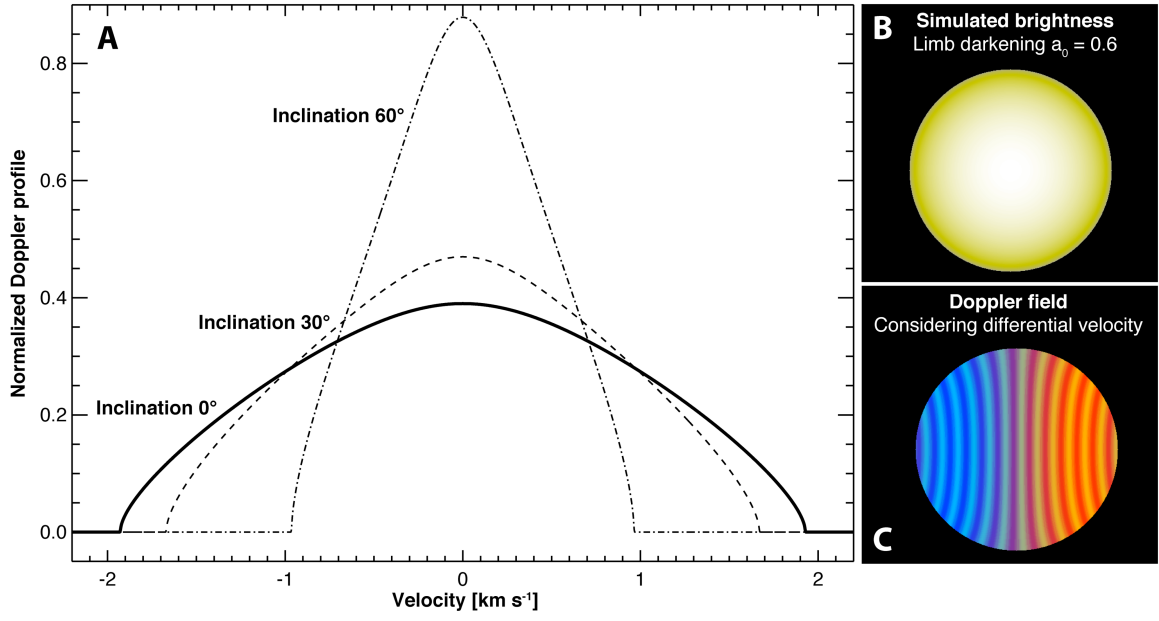
1



2

**Figure B-2.** Comparison of measured and synthetic solar spectra. Trace ‘a’ was synthesized adopting 237 solar lines listed in the Hase et al. [2006] atlas and utilizing 4 parameters per line (center, strength, width and shape parameter). Trace ‘b’ is the solar spectrum as measured with the ATMOS instrument from the Space Shuttle, while ‘c’ is the solar spectrum as measured with the ACE instrument onboard SCISAT-1. Trace ‘c’ is the spectrum modeled by Kurucz [1997], with spectral lines included; it clearly does not reproduce the observed spectra (b, c). For clarity purposes, trace ‘b’ was shifted vertically by -0.1, trace ‘c’ by -0.2 and trace ‘d’ by -0.3.

11



1

2 **Figure B-3. A.** Considered solar rotation Doppler profiles for different inclinations  
 3 relative to the rotation plane. These profiles are used to transform the synthetic disk-  
 4 center spectra by Hase et al. [2006] to disk-integrated spectra at different inclinations in  
 5 the solar system. **B.** Simulated line intensity considered a limb darkening coefficient  $a_0$  of  
 6 0.6. **C.** Doppler field computed considering latitude differential velocity using  
 7 coefficients retrieved from Doppler measurements [Snodgrass and Ulrich, 1990]. Blue  
 8 colors indicate motion towards the observer, while red colors indicate motions away from  
 9 the observer. Yellow vertical lines are traces of iso-velocity.

10

11

1    **Appendix C: General Fluorescence Model (GFM)**

2    We require 11 parameters from the HITRAN database to compute g-factors: molecular  
3    identification (M), isotopologue number (I), frequency of the transition ( $\nu$  [ $\text{cm}^{-1}$ ]),  
4    Einstein A-coefficient ( $A_{21}$  [ $\text{s}^{-1}$ ]), lower state energy ( $E''$  [ $\text{cm}^{-1}$ ]), upper and lower global  
5    vibrational quantum numbers ( $V'$ ,  $V''$ ), upper and lower local rotational quantum numbers  
6    ( $L'$ ,  $L''$ ), and upper and lower statistical weights ( $w'$ ,  $w''$ ). (To avoid confusing  
7    fluorescence emission rates (g-factors) with statistical weights, we use the letter ‘w’  
8    instead of the standard terminology, ‘g’) to refer to the latter). Even though Einstein A-  
9    coefficients can be computed from absorption line intensities [Šimečková et al. 2006], the  
10   inclusion of A-coefficients in HITRAN since 2004 (which replaced the weighted square  
11   of the transition moment) has been a great advance, and is of significant value to studies  
12   related to non-LTE processes.

13   In computing line-by-line fluorescence efficiencies (g-factors) we need to build a full  
14   quantum mechanical model for a molecular band. We illustrate that process for  $\text{C}_2\text{H}_6$ . In  
15   the following sections we present how we (a) create the ro-vibrational structure of the  
16   energy levels, (b) compute the total partition function ( $Q_{\text{tot}}$ ), (c) calculate pumping rates,  
17   and (d) calculate emission rates.

18

19   ***C.1. Re-creation of the ro-vibrational energy-levels***

20   The ro-vibrational structure of the energy levels involved in a particular band system can  
21   be straightforwardly retrieved from the information of the individual lines in the  
22   HITRAN database (however, it is important to validate the numbers because numerous

1 errors exist in the database). For example, by isolating lines from a defined band, and  
2 using 6 parameters ( $v$ ,  $E''$ ,  $L'$ ,  $L''$ ,  $w'$ ,  $w''$ ) for each line, we can recreate an indexed  
3 rotational structure (energy) of the lower and upper states:  $E''(L'') = E_i''$ ;  $E'(L') = E_i'' +$   
4  $v$ ; where  $i$  is the line index, and  $L'$  and  $L''$  refer to the local quantum numbers for the  
5 levels that is determined by the rotational structure. For linear molecules like CO (carbon  
6 monoxide) and  $C_2H_2$  (acetylene), the local quantum number is described by a single value  
7 ( $L = J$ , where  $J$  is the total angular momentum); for symmetric tops  $L = (J, K, \ell)$  (e.g.  
8  $C_2H_6$ ); for molecules like HDO (a prolate asymmetric top) the structure is stored in a  $E(J,$   
9  $K_a, K_c)$  array and the local quantum numbers would be  $L = (J, K_a, K_c)$ .

10

## 11 ***C.2. Computation of the partition function***

12 Computation of the total partition function ( $Q_{\text{tot}}$ ) is particularly difficult, requiring  
13 complete knowledge of all electronic, vibrational, and rotational modes. In the seminal  
14 paper by Gamache et al. [1990], this problem was addressed for a limited set of linear  
15 molecules in the 70-3000K range; the first step in the development of the now widely  
16 used TIPS (Total Internal Partition Sums) program. This study has now been extended to  
17 the full database, and currently the HITRAN database provides total partition sums for all  
18 molecules and isotopologues present in the database for the 70-3000 K temperature range  
19 [Goldman et al. 2000, Fischer et al. 2003, see Pine and Rinsland 1999 for  $C_2H_6$ ].

20 For temperatures lower than 70K, we have considered an analytical approach where we  
21 compute the vibrational and rotational partition functions independently. By using the  
22 retrieved rotational structure we compute the rotational partition function as:

1

$$Q_r = \sum_{i=L_{\min}}^{L_{\max}} w_i'' \exp(-c_2 E_i''/T) \quad (C-1)$$

2 For most molecules (not C<sub>2</sub>H<sub>6</sub>), the vibrational partition function for temperatures lower  
 3 than 70K can be assumed to be unity, since they are only populated in their lowest  
 4 vibrational/electronic level, and herewith the total partition function can be approximated  
 5 to Q<sub>tot</sub> = Q<sub>e</sub>Q<sub>v</sub>Q<sub>r</sub> ~ Q<sub>r</sub> for low temps. In the case of C<sub>2</sub>H<sub>6</sub> with a low-energy vibrational-  
 6 level at ~289 cm<sup>-1</sup> (Ev<sub>4</sub>, torsional mode), we computed the vibrational partition for  
 7 temperatures lower than 70K as following:

8

$$Q_{vib} = [1 - \exp(-c_2 E_{V4}/T)]^{-1} \quad (C-2)$$

9 ***C.3. Computation of fluorescence pumping rates***

10 Perhaps one of the most valuable elements of spectral line lists is that the selection rules  
 11 are explicitly defined by the existence (or non-existence) of a line. In addition, Hönl-  
 12 London factors and Herman-Wallis effects (which are molecule and band dependent) are  
 13 directly contained in the line intensities and A-coefficients. By iterating through the line  
 14 atlas for each line, we compute the pumping rate (g<sub>pump</sub> [s<sup>-1</sup>]) from the reported A-  
 15 coefficient (A<sub>21</sub>), and add it to the corresponding upper-state population defined in L'  
 16 (J',...) following [Crovisier and Encrenaz 1983, Weaver and Mumma 1984, Šimečková et  
 17 al. 2006]:

18

$$g_{pump}(L') = \sum J_s(v_s) \cdot B_{12} \cdot w'' \exp(-c_2 E''/T) / Q_{tot}(T) \quad (C-3)$$

19

$$A_{tot}(L') = \sum A_{21} \quad (C-4)$$

$$B_{12} = B_{21} \cdot \frac{w'}{w''} \quad (\text{C-5})$$

$$B_{21} = A_{21} \cdot (8\pi h v^3)^{-1} \quad (\text{C-6})$$

$$v_s = (1 - u/c)v \quad (\text{C-7})$$

4 where  $J_s$  is the solar flux ( $[J \text{ s cm}^{-3}]$ , see Appendix B) at the Doppler shifted frequency  $\nu_s$   
 5 of the line (being  $u$  [ $\text{cm s}^{-1}$ ] the relative velocity between the comet and the sun and  $c$  the  
 6 speed of light [ $\text{cm s}^{-1}$ ]),  $B_{12}$  the Einstein coefficient for induced absorption [ $\text{J}^{-1} \text{ s}^{-2} \text{ cm}^3$ ],  
 7  $B_{21}$  the Einstein coefficient for stimulated emission [ $\text{J}^{-1} \text{ s}^{-2} \text{ cm}^3$ ],  $A_{\text{tot}}$  the sum of Einstein  
 8 A-coefficients [ $\text{s}^{-1}$ ] mapping to the upper state, and  $h$  is Planck's constant [ $\text{J s}$ ].

#### 10 C.4. Computation of fluorescence emission rates

11 Once all pumps are computed, the branching ratios for each line ‘i’ are calculated as  
 12  $A_{21}/A_{\text{tot}}$ , and with this cometary fluorescence rates (g-factor) are calculated as:

$$g_i = g_{pump}(L') \cdot \frac{A_{21}}{A_{tot}(L')} \quad (C-8)$$

14 Even though the branching ratios ( $A_{21}/A_{\text{tot}}$ ) are temperature independent, the line-by-line  
 15 pumping rates ( $g_{\text{pump}}$ ) are not, and thus g-factors must be computed for every line at the  
 16 appropriate temperature.